JGR Atmospheres

RESEARCH ARTICLE
10.1029/2025JD044231

Turbulent Exchange of CO_2 in the Lower Tropical Troposphere Across Clear-to-Cloudy Conditions

V. S. de Feiter[1], M. Janssens[1], S. E. M. de Haas[1], O. K. Hartogensis[1], C. Q. Dias-Junior[2], H. van Asperen[3], G. Martins[4], J. B. Miller[5], and J. Vilà-Guerau de Arellano[1]

[1]Meteorology and Air Quality Section, Wageningen University & Research, Wageningen, The Netherlands, [2]Physics Department (IFPA), Federal Institute of Pará, Belém, Brazil, [3]Biogeochemical Processes Department, Max Planck Institute for Biogeochemistry, Jena, Germany, [4]Instituto Nacional de Pesquisas da Amazônia, Manaus, Brazil, [5]NOAA/ESRL Global Monitoring, Boulder, CO, USA

Abstract This study investigates the roles of clear air entrainment and shallow cloud ventilation, alongside rainforest CO_2-assimilation, in the turbulent exchange of CO_2 within the lower tropical troposphere under clear-to-cloudy conditions. Constrained by comprehensive observations from the CloudRoots-Amazon22 campaign, spanning leaf stomatal to upper atmosphere, we design and evaluate a representative shallow convective numerical experiment with the turbulence-resolving Dutch Atmospheric Large Eddy Simulation model, incorporating a bulk rainforest representation. We assess contributions from the rainforest, clouds, and environment through the vertically integrated, domain-averaged CO_2 budget by comparing simulations with and without the dynamic effects of clouds. Our findings reveal three distinct diurnal regimes named: entrainment-diluting, cloud-ventilation-and-entrainment, and CO_2-assimilation. Shallow convective clouds (~23%), clear air entrainment (~21%), and rainforest CO_2-assimilation (~56%) collectively influence the diurnal evolution and vertical exchange of CO_2 within the clear-to-cloudy boundary layer, with their relative importance varying per diurnal regime. In the absence of clouds, ventilation ceases and CO_2 exchange is driven solely by entrainment and CO_2-assimilation, resulting in a 20%–25% reduction in mixing effectiveness. In the vertical, shallow clouds ventilate CO_2 to heights reaching twice the boundary layer depth, significantly affecting the vertical distribution until late afternoon. Analysis of the correlation between CO_2 and H_2O shows that shallow convective clouds organize the turbulent exchange at shallow cloud-scales, shaping a vertical pattern of negative to positive CO_2-H_2O correlation from the roughness sublayer into the cloud layer. These findings highlight key processes crucial for accurately representing the lower tropical tropospheric CO_2 budget across clear-to-cloudy conditions.

Plain Language Summary Understanding climate change requires a full picture of how carbon dioxide (CO_2) behaves in the atmosphere, particularly over tropical rainforests such as the Amazon, where interactions between the atmosphere and rainforest are strongest. To capture this behavior, we must study the system from the rainforest to the upper atmosphere. Although progress has been made in understanding how rainforests exchange CO_2, major uncertainties remain; especially when clouds are present. Clouds significantly affect how CO_2 moves in the lower atmosphere compared to clear conditions. To investigate this further, we combined detailed observations from the 2022 CloudRoots-Amazon22 campaign with a high-resolution model that simulates turbulence and clouds. After a thorough validation of the simulation, our results show that clouds and the clear air environment actively shape the behavior of CO_2. During daytime, we identified three distinct periods in the daily cycle that describe CO_2 movement when clouds start to form in an initially clear sky. Vertically, clouds transport CO_2 from near the surface up to heights of 3.5 km. Moreover, clouds not only lift CO_2 but also organize how it moves upward. This research highlights key processes that are crucial for accurately understanding and representing CO_2 dynamics in the atmosphere above tropical rainforests.

Key Points:

- Shallow convective cloud ventilation and clear air entrainment collectively shape the clear-to-cloudy boundary layer CO_2-exchange
- Shallow convective clouds influence the vertical CO_2 distribution until late afternoon, reaching heights twice the boundary layer depth
- Shallow convective clouds shape a strong vertical negative-to-positive CO_2-H_2O correlation at shallow cloud-scales

Supporting Information:

Supporting Information may be found in the online version of this article.

Correspondence to:

V. S. de Feiter,
vincent.defeiter@wur.nl

Citation:

de Feiter, V. S., Janssens, M., de Haas, S. E. M., Hartogensis, O. K., Dias-Junior, C. Q., van Asperen, H., et al. (2025). Turbulent exchange of CO_2 in the lower tropical troposphere across clear-to-cloudy conditions. *Journal of Geophysical Research: Atmospheres*, *130*, e2025JD044231. https://doi.org/10.1029/2025JD044231

Received 1 MAY 2025
Accepted 13 SEP 2025

1. Introduction

Obtaining a full understanding of anthropogenic climate change necessitates a thorough understanding of the diurnal (daytime, between sunrise and sunset) and vertical variability of atmospheric carbon dioxide (CO_2) above tropical rainforests such as the Amazon, the largest terrestrial carbon sinks on our planet (Anav et al., 2015; Friedlingstein et al., 2023). Although significant progress has been made in quantifying rainforest carbon exchange and its response to extreme weather events such as droughts and heatwaves (e.g., Alden et al., 2016; Gatti

et al., 2014; van der Laan-Luijkx et al., 2015), uncertainties remain in estimates of these surface exchange fluxes, largely due to limited observations and limitations in accurately representing the atmospheric processes involved in the CO_2 exchange (Bastos et al., 2020; Botía et al., 2022).

Among the atmospheric processes governing CO_2 exchange, moist convection remains particularly unexplored. Previous work has emphasized the importance of biospheric to atmospheric fluxes of photosynthesis and respiration (e.g., Fitzjarrald et al., 1990; Garstang & Fitzjarrald, 1999), dry convection (e.g., Hooft et al., 2019; Pino et al., 2012), and horizontal advection (e.g., Botía et al., 2022; Pino et al., 2013). However, the contribution of moist convective processes to the CO_2 budget and subsequently the errors arising from misrepresentating these processes, remain elusive. Particular attention should be given to the role of shallow moist convection, which is a characteristic feature above tropical ecosystems such as the Amazon during the dry season (Giangrande et al., 2020).

During the morning, the clear boundary layer above the dry season rainforest surface typically transitions to a layer topped by small, active, and non-precipitating shallow convective clouds (<2 km in depth) (Giangrande et al., 2020; Henkes et al., 2021). These active clouds are closely coupled to the forest (Gentine et al., 2019). Hence, shallow moist convection is thought to significantly influence and connect the diurnal cycles of energy, water, and atmospheric CO_2 in the lower troposphere (Gentine et al., 2019; Sikma & Vilà-Guerau de Arellano, 2019; Vilà-Guerau de Arellano et al., 2020). To place such ideas on more quantitative grounds, we will study the contributions of dry and moist convection, alongside CO_2-assimilation by the Amazon rainforest, in shaping the diurnal and vertical variability of atmospheric CO_2 in the lower tropical troposphere.

To more specifically motivate how shallow moist convection might influence the vertical variability of CO_2 over the Amazon, we present aircraft observations from the recent CloudRoots-Amazon22 measurement campaign (Vilà-Guerau de Arellano et al., 2024) (Figure 1). During this campaign, held at the Amazon Tall Tower Observatory (ATTO) and Campina measurement site (Andreae et al., 2015), an aircraft equipped with Piccaro gas analyzers, flew a vertical profile combined with three horizontal rasters with a distance of 20 km in the early afternoon (13 hr Local Time (LT) = UTC–4 hr) on the 18th of August 2022, where non-precipitating shallow convective clouds formed from the late morning onward. The horizontal levels were distributed throughout the lower troposphere: in the roughness sublayer (low (L), z_L at ∼200 m), subcloud layer (medium (M), z_M at ∼1,100 m), and cloud layer (high (H), z_H ∼ 3,000 m). For simplicity the height of the subcloud layer is taken synonymous to the well-mixed boundary layer height when shallow convective clouds are present (well-mixed boundary layer height (z_i) at ∼1,500 m as measured by a ceilometer). During the flight, the aircraft measured mole fractions of $\varphi \in [CO_2, H_2O]$ in the environment; the aircraft did not fly through the clouds themselves.

In Figure 1 we visualize the linearly detrended correlation between fluctuations (φ') in H_2O and CO_2 around spatial raster-averages ($\overline{\varphi}$). The figure shows that $CO_2{}'$ and H_2O' are correlated at each height and that this correlation changes with height. In the roughness sublayer, a region that is still influenced by the rainforest, CO_2 and H_2O are negatively correlated (Pearson correlation coefficient (r) = −0.3), with larger $CO_2{}'$ compared to H_2O'. Higher up in the cloud layer (3,000 m), CO_2 and H_2O are strongly positively correlated (r = 0.95), as variability in CO_2 decreases, whereas variability in H_2O increases. In between, in the upper part of the subcloud layer (z_M), the correlation is also negative (r = −0.51), although there is a considerable variability in both H_2O and CO_2.

The vertical transition from negative to positive CO_2-H_2O correlation up to z_i was previously noted by Vilà-Guerau de Arellano et al. (2004) above grassland at Cabauw (The Netherlands), under non-cloudy conditions. They concluded that near the surface, CO_2 mole fractions decrease through descending motions induced by photosynthesis (CO_2-assimilation), whereas ascending convective thermals originating from the surface are moistened from below through evapotranspiration, creating a strong negative correlation in the roughness sublayer. Near z_i, the CO_2 and moisture in an ascending thermal originating from the surface will have relaxed toward typical boundary layer CO_2 mole fractions through lateral mixing. Since the ambient CO_2 and moisture generally reduce with height around z_i, a thermal with bulk-boundary layer moisture and CO_2 will possess both a CO_2 and moisture excess. Conversely, compensating descending motions from the free troposphere will contain both less CO_2 and moisture. Hence, when both the CO_2 and moisture gradients with height are negative, as is often the case at z_i and in the lower free troposphere, we expect both clear and cloudy circulations to generate positive CO_2-moisture correlations around z_i. However, in the observations displayed in Figure 1, a positive correlation is found

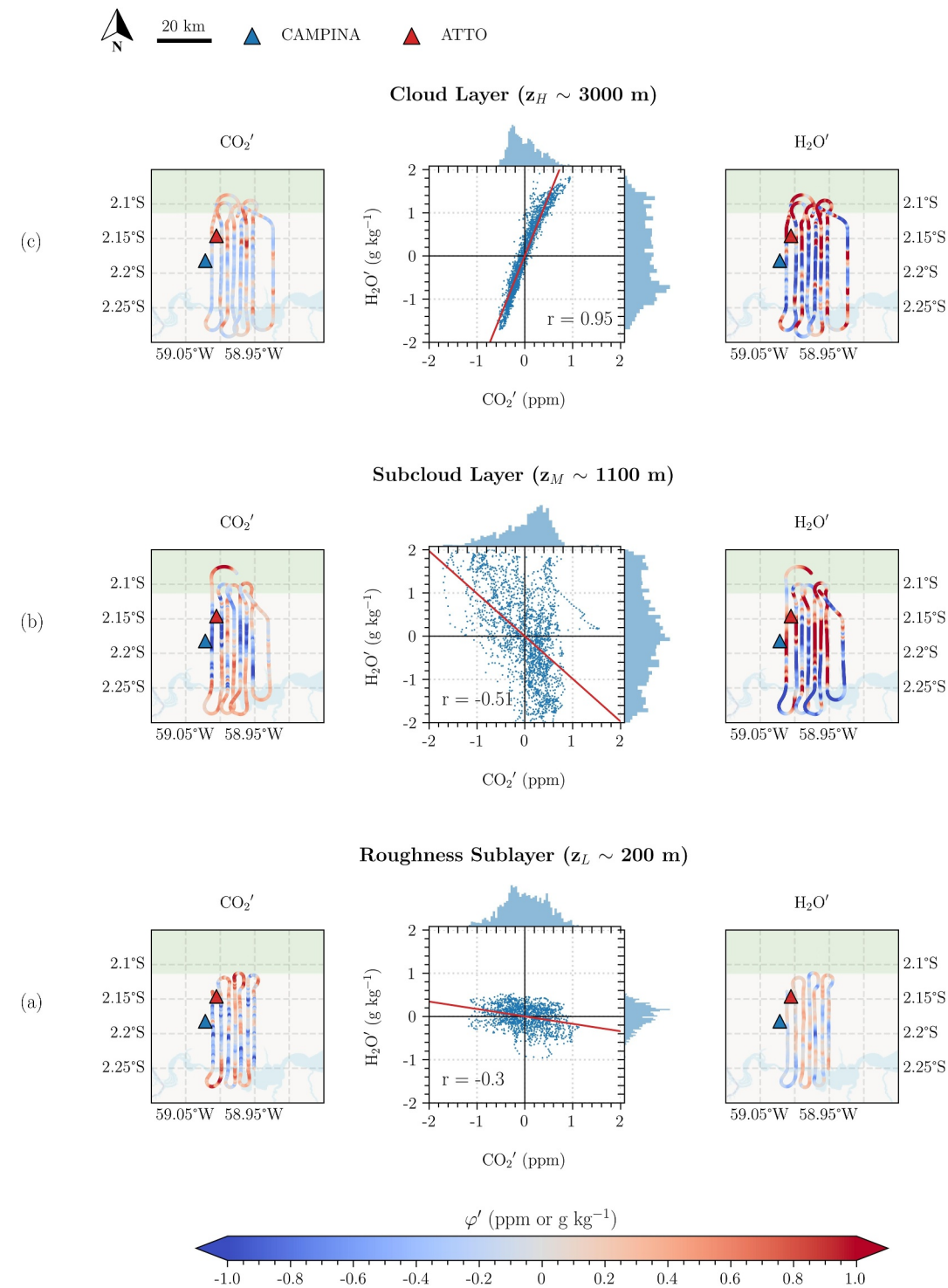

Figure 1. Observed linearly detrended correlation between fluctuations (φ') in CO_2 and H_2O around spatial raster-averages ($\overline{\varphi}$) and the corresponding Pearson correlation coefficient (r) at 13 LT across three heights: (a) z_L (roughness sublayer at ~200 m), (b) z_M (subcloud layer at ~1,100 m) and (c) z_H (cloud layer at ~3,000 m). Note that for simplicity the height of the subcloud layer is taken synonymous to the well-mixed boundary layer height when shallow convective clouds are present (well-mixed boundary layer height (z_i) at ~1,500 m as measured by a ceilometer). Basemap: OpenStreetMap, with water (blue), terra firm (brown), and rainforest (green). Triangular markers indicate the location of the Amazon Tall Tower Observatory (ATTO) and Campina measurement site.

far above z_i, in the shallow cloud layer, suggesting that shallow convective clouds may play a role in extending this vertical positive correlation.

Shallow convective clouds can transport ("vent") volumes of air from the subcloud layer into the cloud layer and across the lower troposphere via upward mass fluxes (M) (Nicholls & Lemone, 1980; Ouwersloot et al., 2013; van Stratum et al., 2014). This venting typically dries out and limits the growth of z_i, whereas also influencing the atmospheric residence time of transported gases (Bardakov et al., 2022; Lu et al., 2000). Simultaneously, shallow convective clouds facilitate downward transport to the surface ("pump"), both locally, through subsiding shells around the clouds and across broader regions via compensating subsidence (Jonker et al., 2008; McMichael et al., 2020; Rodts et al., 2003). Consequently, these venting and pumping characteristics raise the question whether the strong positive CO_2-H_2O correlation within the cloud layer reflects upward CO_2 transport via moist cloudy mass fluxes and downward transport through clear skies, and whether this correlated signal is present and remains throughout the day when we move from clear (dry convective) to cloudy (moist convective) conditions. More concretely, Figure 1 motivates us to formulate three research questions:

1. How do cloud ventilation by shallow convective clouds, clear air entrainment, and rainforest CO_2-assimilation collectively regulate the turbulent exchange of atmospheric boundary layer CO_2 across clear-to-cloudy conditions?
2. How does cloud ventilation by shallow convective clouds influence the vertical distribution of CO_2 in the lower tropical troposphere?
3. What role does shallow moist convection play in shaping the vertical correlation pattern between CO_2 and water vapor, as illustrated in Figure 1?

To address these questions, we combine observations from the CloudRoots-Amazon22 campaign to design and analyze a Large Eddy Simulation (LES) experiment for a typical non-precipitating shallow convective day in the Amazonian dry season. We run two simulations: one standard with clouds and one mechanism-denial experiment without clouds, where condensation is prevented from affecting model dynamics. The observations and details of the numerical experiment are introduced in Section 2. We first validate the simulation in Section 3.1. Next, we examine and discuss the role entrainment (dry convection) and mass fluxes (moist convection), alongside rainforest CO_2-assimilation, in the CO_2 budgets of the clear-to-cloudy boundary layer (Section 3.2) and lower troposphere (Section 3.3). Furthermore, we examine whether turbulence and shallow convective clouds organize vertical exchange of CO_2 as represented in Figure 1 (Section 3.4). Lastly, we summarize the key findings in Section 4.

2. Material and Methods

2.1. CloudRoots-Amazon22 Campaign

The CloudRoots-Amazon22 campaign (Vilà-Guerau de Arellano et al., 2024) was conducted between the 8th to 21st August 2022 (dry season) at the Amazon Tall Tower Observatory (ATTO) (lat: −2.1458°, lon: −59.0055°) and Campina (lat: −2.1819°, lon: −59.0217°) measurement sites located in central Amazon (Andreae et al., 2015). During the campaign, aimed at studying rainforest-atmosphere exchange across the ∼40 m tall canopy and lower troposphere, continuous measurements of soil properties and atmospheric state variables (including CO_2 mole fractions), along with their turbulent fluxes, were conducted on and around two towers of 323 and 81 m height (Vilà-Guerau de Arellano et al., 2024). The vertical domain was expanded by releasing daily radiosondes at a three-hour interval (6, 9, 12, 15, and 18 LT (LT = UTC−4 hr)). Additionally, on the 18th of August 2022, an aircraft measured vertical profiles (up to 5 km) of both CO_2 and humidity, and flew the 20 km rasters presented in Figure 1. In addition to the afternoon (13 LT) flight presented in Figure 1, aircraft observations were also collected during the morning (9 LT).

To initialize and evaluate our LES experiment, we use the following observations. First, we combine the meteorological state variables and CO_2 mole fractions from the towers, radiosondes, and aircraft into connected vertical profiles from within the canopy to the mid-troposphere according to their availability. In addition, we infer the boundary layer height (z_i) from the observed backscattering of a permanently installed ceilometer at Campina and from the available radiosondes. Regarding the radiosondes, we follow well-mixed theory and z_i is taken as the height where fits of a constant well-mixed potential temperature value, derived from the lowest levels of the connected vertical profiles, intersects a linear fit of the free-tropospheric lapse rate of potential temperature

(e.g., Lilly, 1968; Pino et al., 2006). Additionally, we evaluate simulated clouds against reflectivity, type, base, thickness and top retrieved from a MIRA Doppler cloud radar. The ceilometer and MIRA radar did not operate on the 17th of August 2022, and thus data for this day is missing.

Based on the observations, visual inspection of available time-lapse imagery from an upward looking camera at ATTO, and previous characterization studies (e.g., Henkes et al., 2021), data from the CloudRoots-Amazon22 campaign were categorized into two convective regimes based on the type of clouds that developed throughout the day: shallow convective (6 days, 9, 10, 11, 15, 17, and 18 of August 2022) and shallow-to-deep convective (4 days, 12, 13, 14, and 16 of August 2022) (Vilà-Guerau de Arellano et al., 2024). This study focuses solely on observations from the shallow convective regime.

2.2. Numerical Simulation

Simulations of meteorological state variables and CO_2 are performed with the Dutch Atmospheric Large Eddy Simulation (DALES) (Heus et al., 2010; Ouwersloot et al., 2017), version 4.4. The simulation design builds on the Green Ocean Amazon 2014/15 case studied by Vilà-Guerau de Arellano et al. (2020). Its domain spans 19×19 km horizontally ($\Delta x = \Delta y = 53$ m) to match the aircraft raster size, and 5 km vertically ($\Delta z = 20$ m). The model is run for 12 hr ($\Delta t = 1$ s) between 6 and 18 LT and is horizontally constrained by doubly periodic boundaries, where the first hour is considered spin-up. In the vertical, the bottom surface is forced by a coupled land surface model, whereas the top of the domain contains a sponge layer (Heus et al., 2010). The sponge layer is a relaxation toward the top of the domain in which we dampen the fluctuations of state variables and CO_2 generated by clouds and turbulence in the upper part of the domain around their mean state to prevent numerical instability. For our simulation, we consider the upper 25% (between 3.75 and 5 km) of the domain for the sponge layer, which is at a sufficient height from the shallow convective cloud tops (at a height of ∼3 km, Figure 2c) in order to not intervene with their development.

The land surface model is a CO_2-assimilation (A) represented by stomatal conductance (g_s) A-g_s model (Pedruzo-Bagazgoitia et al., 2017; Ronda et al., 2001), constrained to the phenological observations taken during CloudRoots-Amazon22 (González-Armas et al., 2025; Vilà-Guerau de Arellano et al., 2024). The g_s represents the stomatal aperture or opening of the stomata, controlling the in- or outflow of CO_2 and H_2O in the A-g_s scheme. The stomatal aperture depends on environmental conditions such as photosynthetically active radiation, temperature and vapor pressure deficit, which feed back into the surface energy and CO_2 fluxes (Ronda et al., 2001). For the A-g_s scheme a single sunlit big-leaf representation is used for each grid cell as a simplified representation of all individual leaves of the rainforest in the horizontally homogeneous domain. The A-g_s scheme is upscaled and incorporated into a bulk (vertically integrated) rainforest canopy representation. Additionally, the daytime respiration is fixed at 5.18 μmol m^{-2} s^{-1} as observations displayed near-constant respiration at this rate (Figure S1 in Supporting Information S1). For radiation, we use a one-dimensional Rapid Radiative Transfer Model for Global circulation (RRTMG) (Iacono et al., 2008), calculating partitioning of radiation into direct and diffuse radiation (including photosynthetically active radiation) at each column of the model. Consequently, cloud shadows are projected directly below the cloud.

Although using a sunlit big-leaf approach and the one-dimensional RRTMG scheme may lead to misrepresentations of the meteorology and subsequent surface fluxes such as CO_2-assimilation, our DALES simulation shows to reproduce the radiation, boundary layer development, meteorological state variables, and surface fluxes satisfactorily compared to the CloudRoots-Amazon22 observations (Figures 2 and 3, Section 3.1). Therefore, we expect any discrepancies arising from these model settings to be negligible for assessing the diurnal and vertical variability of CO_2 in the clear-to-cloudy lower troposphere.

Within the LES domain, CO_2 is advected with the resolved and unresolved flow as an inert tracer. Model grid boxes are either entirely cloudy or cloud-free, and condensation affects the local thermodynamics by instantaneous saturation adjustment ("all or nothing" cloud adjustment scheme (Heus et al., 2010)). All rain microphysics are disabled, as we investigate non-precipitating shallow convective clouds.

We initialize the simulation with vertical profiles of potential temperature (θ), specific humidity (q), and horizontal winds (u, v) averaged (aggregated) over the six observed shallow convective days of CloudRoots-Amazon22 (Vilà-Guerau de Arellano et al., 2024), at 6 LT. For CO_2, an initial vertical profile is constructed from the morning vertical flight profile (9 LT) above z_i (vertical (initial) profiles of θ, q, CO_2, u, and v are

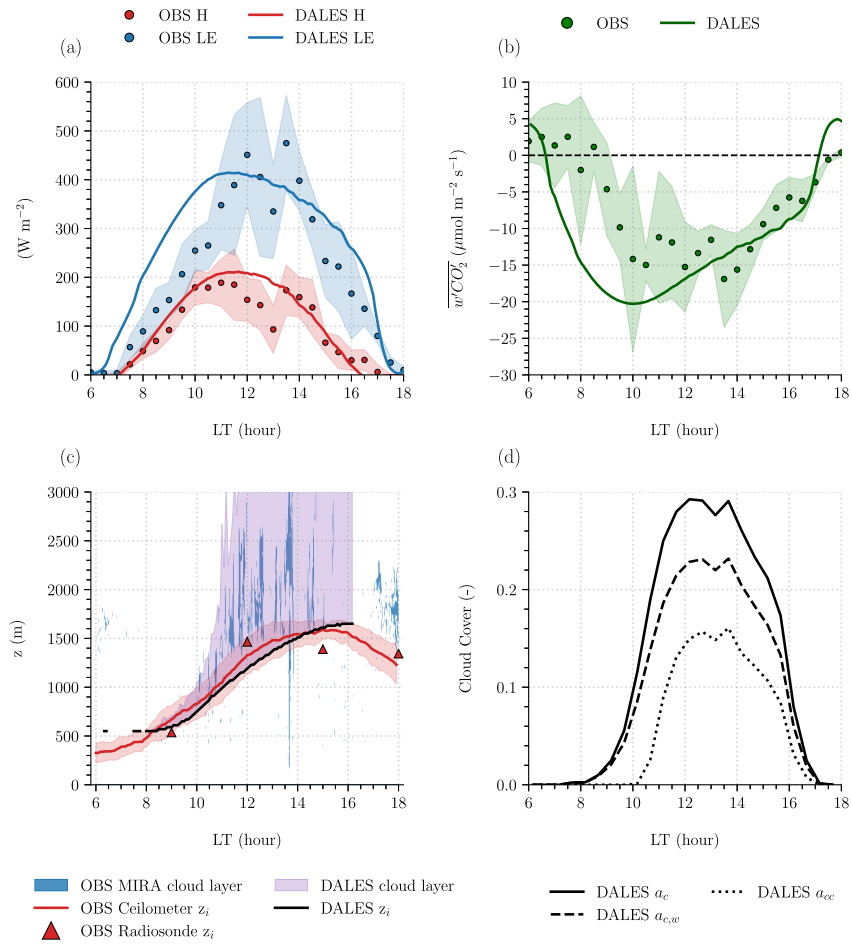

Figure 2. Observed (markers) and simulated (solid line) 6-day aggregated diurnal evolution of (a) rainforest surface fluxes—sensible (H) and latent heat flux (LE), (b) CO_2 surface flux $\left(\left(\overline{w'CO_2'}\right)_s\right)$–at 10 m above canopy top ($z = 50$ m), along with (c) 6-day aggregated diurnal development of the clear-to-cloudy boundary layer (z_i), cloud layer and cloud onset, and (d) the diurnal evolution of the simulated mean cloud fraction, split into the three criteria: cloud-average cloud fraction (a_c, where $q_l >$ 0 g kg^{-1}), upward-moving cloud-average cloud fraction ($a_{c,w}$, where $q_l > 0$ g kg^{-1}, $w' > 0$ m s^{-1}) and core-average cloud fraction (a_{cc}, where $q_l > 0$ g kg^{-1}, $w' > 0$ m s^{-1} and $\theta_v' > 0$ K). Markers indicate the observed 6-day aggregated diurnal behavior for days on which shallow convective clouds were observed, whereas the shaded areas represent the spread of one standard deviation during the six observed shallow convective days. For DALES, z_i is set equal to the height of the minimum buoyancy flux.

presented in Supplementary Figures S2 and S3 in Supporting Information S1). Below z_i, tower CO_2 data suggest that increased CO_2 mole fractions (>450 ppm) from respiration in the early morning (6−10 LT), which are transported upward (flushed-up) from near the surface as turbulence initiates during the morning transition (Culf et al., 1997; Dupont et al., 2024; González-Armas et al., 2025) (Figure 3d). Our bulk canopy approach cannot directly represent these in-canopy motions which create this flush-up. The A-g_s scheme misses a method for representing the morning transition in which we move from nighttime respiration to the daytime assimilation. Consequently, assimilation activates immediately after the spin up of the simulation. To ensure that we do simulate realistic conditions by the time the flush-up is completed, we manually enhance the inversion strength from the 9 LT profile in our initial profile based on the tower (24, 38, 53, 79, and 321 m) observations, matching near-canopy (53 m) observations and attaining a realistic well-mixed CO_2 mole fraction in the course of the day. The selected values of the phenological and model parameters, model settings, and initial profiles used for the simulations are accessible via the supporting code and data repository (de Feiter et al., 2025).

To isolate the role of shallow convective clouds, we impose no domain-averaged horizontal advection and vertical advection, assuming a zero large-scale vertical velocity. We also conduct two simulations; one with and one

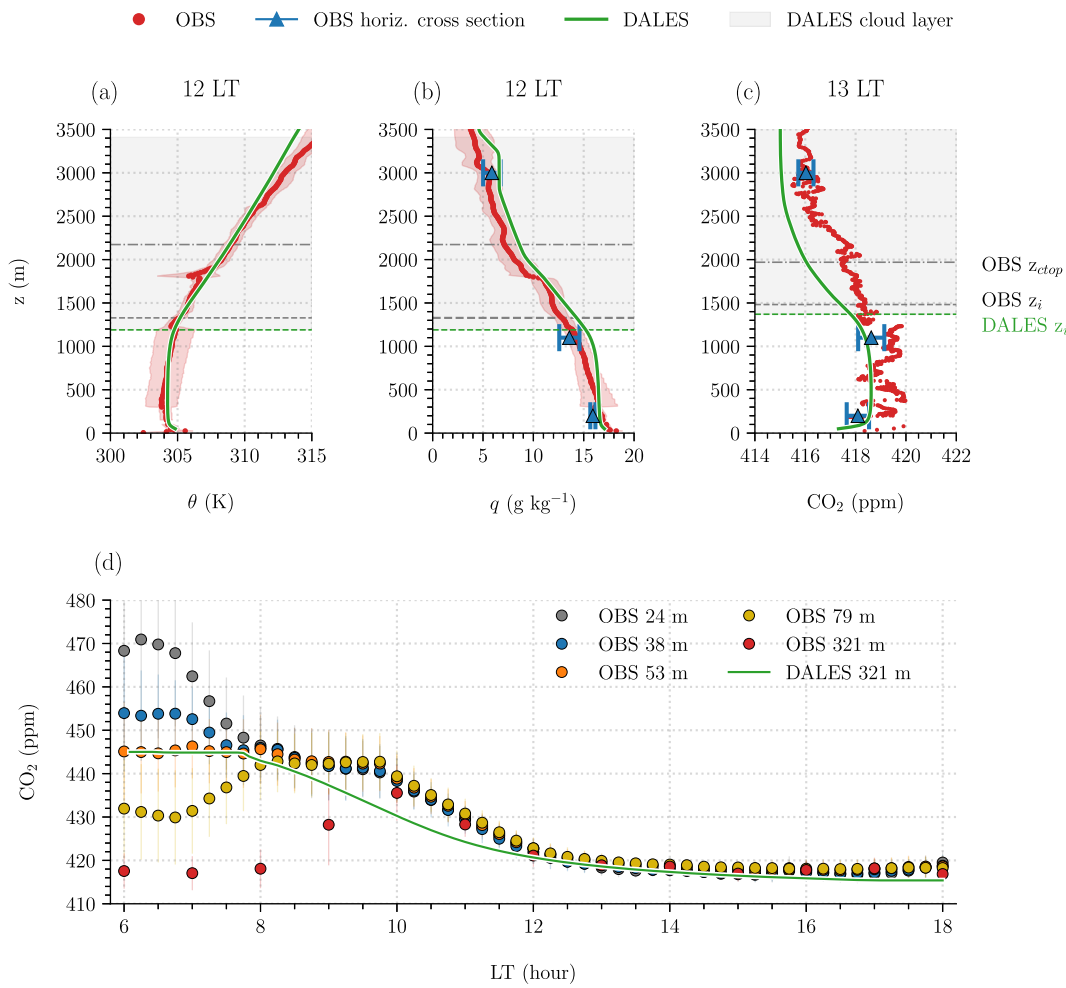

Figure 3. Observed (markers) and simulated (solid line) vertical profiles at 12 and 13 LT: (a) potential temperature (θ) and (b) specific humidity (q) from daily radiosonde observations and (c) CO_2 from aircraft observations on the 18th of August 2022. Markers indicate the mean profile, whereas the shaded areas represent the spread of one standard deviation during the six observed shallow convective days. The observed vertical profiles combine tower and radiosonde data, explaining the lower standard deviation in the lower 300 m. Blue horizontal markers represent the horizontal cross sections as measured by the aircraft at 13 LT on the 18th of August 2022, horizontal dashed or dashed-dotted lines represent the observed (gray lines) and simulated (green line) z_i and average cloud top at ATTO (z_{ctop}), respectively. Additionally, (d) shows the diurnal evolution of CO_2, observed (marker) and simulated (green line) mole fraction at 24, 38, 53, 79, and 321 m between 6 and 18 LT. Markers indicate the mean observations, whereas the error bars denote the spread of one standard deviation during the six observed shallow convective days.

without dynamically active shallow convective clouds as a mechanism-denial experiment, where condensation of water vapor in clouds does not influence the radiation and thermodynamic calculations; the latent heat of vaporization is set to zero. These simulations are referred to as `CLOUDS` and `NO CLOUDS`, respectively. Model output consists of both 1D (t,z) horizontally averaged 5-min statistics and 3D (t,x,y,z) 5-min instantaneous data at the grid scale. The 1D data include contributions toward vertical fluxes from the subgrid-scale model; the 3D data do not. A comparison of 30-min averaged 1D and 3D data reveal no significant differences vertically across the lower troposphere (Figure S4 in Supporting Information S1). Consequently, both data sets are used throughout the following analysis.

2.3. Budget Analysis

To quantify the contributions of shallow convective clouds, clear air entrainment and the rainforest CO_2-assimilation to the diurnal (daytime, between sunrise (6 LT) and sunset (18 LT)) and vertical (0–5 km) variability

of CO_2 above the Amazon, we study various decompositions of the atmospheric CO_2 budget with our LES simulations during the day. These analyses depart from the horizontally averaged vertically resolved CO_2 budget in the Boussinesq approximation (Equation 1) (Betts et al., 1990; Ouwersloot et al., 2013; Stull, 1988). Here, the terms represent the CO_2-tendency (first term), mean horizontal (second and third term) and vertical advection (fourth term) of CO_2, and the vertical divergence of the CO_2 flux (fifth term). These terms balance at all levels above the surface in the absence of external sources and sinks such as photosynthesis or respiration. The different terms within Equation 1 and the subsequent equations in this section are presented as 30-min averages directly determined from the 1D and 3D simulation outputs.

$$\frac{\partial \overline{CO_2}}{\partial t} + \overline{u}\frac{\partial \overline{CO_2}}{\partial x} + \overline{v}\frac{\partial \overline{CO_2}}{\partial y} + \overline{w}\frac{\partial \overline{CO_2}}{\partial z} + \frac{\partial}{\partial z}\overline{w'CO_2'} = 0 \tag{1}$$

Since horizontal and vertical advections (subsidence) are neglected in our LES, Equation 1 can be simplified to Equation 2:

$$\frac{\partial \overline{CO_2}}{\partial t} = -\frac{\partial}{\partial z}\overline{w'CO_2'} + R \tag{2}$$

Here R represents a residual term, which appears in the following as a result of errors made by (a) time-interpolating $\overline{CO_2}$ when estimating its time derivative, and (b) ignoring the subgrid contributions to $\overline{w'CO_2'}$ in our a-posteriori estimates of the budget.

2.3.1. Clear-to-Cloudy Boundary Layer CO_2 Budget

To answer the first research question, we study the vertically averaged clear-to-cloudy boundary layer CO_2 budget over time (Section 3.2). With clear-to-cloudy we refer to clear boundary layers that become cloudy due to the formation of shallow convective clouds throughout the day. The formulation of the budget follows from vertically integrating Equation 2 (ignoring R at present) from the canopy top, in DALES taken to be the lower surface ($z_c = 0$ m), to the top of the well-mixed boundary layer (z_i) and dividing by z_i. For simplicity, the subcloud layer height is taken synonymous with z_i when shallow convective clouds are present, reducing additional complexity involved in analyzing the dynamics of the transition from unsaturated to saturated air (Albright et al., 2022). For DALES, z_i is set equal to the height of the minimum buoyancy flux. Defining $\langle\cdot\rangle$ as the vertical average, we obtain Equation 3 for the budget of boundary layer CO_2 in DALES, $\langle\overline{CO_2}\rangle$, where $\left(\overline{w'CO_2'}\right)_s$ is the flux of CO_2 at z_c, which is proportional to the net ecosystem exchange estimated by the A-g_s model, and $\left(\overline{w'CO_2'}\right)_e$ representing the net flux at z_i, the interface between the clear-to-cloudy boundary layer and free troposphere.

$$\frac{\partial \langle\overline{CO_2}\rangle}{\partial t} = \frac{1}{z_i}\int_{z_c}^{z_i}\frac{\partial \overline{CO_2}}{\partial t}dz = \frac{\left(\overline{w'CO_2'}\right)_s - \left(\overline{w'CO_2'}\right)_e}{z_i}, \tag{3}$$

to further disentangle the processes controlling $\langle\overline{CO_2}\rangle$, we expand the fluxes $\left(\overline{w'CO_2'}\right)_s$ and $\left(\overline{w'CO_2'}\right)_e$ into a form more suitable for our subsequent analysis and physical interpretation. First, $\left(\overline{w'CO_2'}\right)_s$ can be expanded based on the CO_2-assimilation (A) and respiration ($Resp$) rates at canopy scale (Equation 4), following the A-g_s model formulation from Ronda et al. (2001). The canopy-scale net CO_2-assimilation ($A_{n,c}$) is obtained by upscaling the net CO_2-assimilation of individual leaves (A_n) (Equation 5). Here A_g represents the gross CO_2-assimilation rate, R_d the dark respiration, $g_{l,c}$ the stomatal conductance at the leaf level, C_i the internal CO_2 mole fraction within the leaf, and C_s the CO_2 mole fraction at the leaf surface equal to the well-mixed atmospheric mole fraction ($C_s = \langle CO_2\rangle$). Upscaling $g_{l,c}$ yields the stomatal conductance at the rainforest canopy level $\left(g_{c,c}\right)$. Substituting $A_{n,c}$ of Equation 5 into Equation 4 and neglecting the aerodynamic resistance yields an approximation of $\left(\overline{w'CO_2'}\right)_s$ (Equation 6). Here, $(\langle CO_2\rangle - C_i)$ can be noted as $\Delta C_{vegetation}$ since it denotes the difference in CO_2 between the atmosphere and the vegetation. Since $Resp$ is approximately constant in time (Figure S1 in Supporting Information S1), the stomatal CO_2-assimilation is the primary factor regulating the diurnal variability in $\left(\overline{w'CO_2'}\right)_s$.

$$\left(\overline{w'\mathrm{CO}_2'}\right)_s = A_{n,c} + Resp \tag{4}$$

$$\overbrace{A_n = A_g - R_d = g_{lc}(C_s - C_i)}^{\text{leaf}} \rightarrow \overbrace{A_{nc} = g_{cc}(\langle \mathrm{CO}_2 \rangle - C_i)}^{\text{canopy}} \tag{5}$$

$$\left(\overline{w'\mathrm{CO}_2'}\right)_s = A_{n,c} + Resp = g_{c,c}(\langle \mathrm{CO}_2 \rangle - C_i) + Resp \approx g_{c,c}\Delta C_{vegetation} \tag{6}$$

Next, we expand $\left(\overline{w'\mathrm{CO}_2'}\right)_e$. Since we wish to quantify the contribution of dry and moist convective processes to $\left(\overline{w'\mathrm{CO}_2'}\right)_e$, we partition the flux by subsetting the DALES grid into the average contribution from clouds and the environment following the "top-hat" approximation commonly used in large scale numerical modeling (Siebesma & Cuijpers, 1995). More concretely, we partition $\left(\overline{w'\mathrm{CO}_2'}\right)_e$ by selecting all vertical grid columns with a cloud present anywhere in the column (superscript `cl`, the in-cloud contribution), and all grid columns which do not have a cloud (superscript `env`, the environment contribution). Assessing the presence of a cloud in the vertical grid column is done using the 2D (x,y) cloud fraction of the DALES grid (a_x) (Equation 7).

$$\left(\overline{w'\mathrm{CO}_2'}\right)_e = \overbrace{a_{cw}\left(\overline{w'\mathrm{CO}_2'}^{cl}\right)_e}^{\text{in-cloud}} + \overbrace{(1 - a_{cw})\left(\overline{w'\mathrm{CO}_2'}^{env}\right)_e}^{\text{environment}} \tag{7}$$

It is important to note that the relative in-cloud and environment contributions to $\left(\overline{w'\mathrm{CO}_2'}\right)_e$ highly depend on the selected cloud fraction. Selecting a different criterion defining the cloud fraction could yield different results. Throughout literature (e.g., Siebesma et al., 2003), two criteria are commonly presented for selecting cloud fractions within model grids: the "cloud-average" (liquid specific humidity $(q_l) > 0$ g kg^{-1}) and the "core-average" ($q_l > 0$ g kg^{-1}, positive fluctuations in vertical velocity $(w') > 0$ m s^{-1} and buoyancy $(\theta_v') > 0$ K compared to the domain average criterion. The cloud-average cloud fraction (a_c) and core-average cloud fraction (a_{cc}) are thereby related through approximately a factor 2 ($a_c \approx 2a_{cc}$) (Sikma & Ouwersloot, 2015).

We anticipate that the ventilation of CO_2 by shallow convective clouds is predominantly driven by actively buoyant, upward-moving regions (updraughts) concentrated within the cloud cores. The dynamics of these buoyant cores can, in turn, generate additional small-scale turbulent motions along their edges, promoting mixing with surrounding neutral or negatively buoyant air through entrainment and detrainment processes (de Rooy et al., 2013; Savre, 2022). Consequently, larger volumes of air, and CO_2, can be transported upward. To account for this process, we introduce a less strict criterion termed the "upward-moving-cloud-average" criterion ($q_l > 0$ g kg^{-1} and $w' > 0$ m s^{-1}), with the upward-moving cloud-average fraction referred to as $a_{c,w}$. Adopting a different criterion primarily impacts how many grid columns are classified as cloud or environment, introducing a sensitivity in the overall contribution by in-cloud and environment grid cells. For completeness, we present the sensitivity of using the different cloud fractions to our main results in Figure S5 in Supporting Information S1.

For more quantitatively associating the partitioned fluxes in Equation 7 with in-cloud venting and clear air entrainment, we rewrite the equation using a well-mixed zero-order jump model formulation over an infinitesimal small layer similar to Equation 6 (Pino et al., 2006). We rewrite the terms as a product of a characteristic vertical velocity (entrainment), and the difference in CO_2 mole fraction between the well-mixed clear-to-cloudy boundary layer mole fraction ($\langle \mathrm{CO}_2 \rangle$) and the free tropospheric mole fraction at 100 m above z_i $\left(C_{ft} \approx C_{z_i+100\ \mathrm{m}}\right)$ (similar to Albright et al., 2022): $\Delta C_{atm} = C_{ft} - \langle \mathrm{CO}_2 \rangle$. We assume $a_{c,w}$ to be negligibly small $(1 - a_{c,w} \approx 1)$ as the organized turbulence dominates the net flux (Siebesma & Cuijpers, 1995). Consequently, the expression for the clear air contribution is reduced to Equation 8, where we diagnose the clear air entrainment velocity w_e as the vertical velocity needed to satisfy the equation.

$$(1 - a_{c,w})\left(\overline{w'\mathrm{CO}_2'}^{env}\right)_e = -w_e \Delta C_{atm}, \tag{8}$$

we write the in-cloud contribution as Equation 9, where we define the convective mass flux ($M = a_{c,w}w_{cloud}$) (e.g., van Stratum et al., 2014), and again define w_{cloud} as the vertical velocity needed to satisfy Equation 9.

$$a_{c,w}\left(\overline{w'CO_2'}^{cl}\right)_e = a_{c,w}w_{cloud}\Delta C_{atm} = M\Delta C_{atm}, \tag{9}$$

taken together, Equations 8 and 9 yield a rewritten and extended version of Equation 7 which we use in Section 3.2 (Equation 10):

$$\overline{w'CO_2'}_e = M\Delta C_{atm} - w_e\Delta C_{atm} \tag{10}$$

By substituting Equations 6 and 10 into Equation 3, we obtain Equation 11:

$$\frac{\partial\langle\overline{CO_2}\rangle}{\partial t} = \overbrace{\frac{Resp}{z_i}}^{(1)} - \overbrace{\frac{g_{c,c}}{z_i}}^{(2)}\Delta C_{vegetation} - \left(\overbrace{\frac{M}{z_i}}^{(3)} - \overbrace{\frac{w_e}{z_i}}^{(4)}\right)\Delta C_{atm} \tag{11}$$

This equation distinguishes between four main terms which influence the diurnal evolution of $\langle\overline{CO_2}\rangle$: respiration (a), rainforest CO_2-assimilation (b), in-cloud ventilation (c), and clear air entrainment (d). Since the respiration term (term 1) is kept constant throughout the diurnal cycle, we mainly examine the relative contribution of terms 2 to 4 as the simulation progresses.

2.3.2. Vertically Resolved CO_2 Budget and CO_2-H_2O Correlation

To study the role of the shallow convection throughout the lower tropical troposphere (Section 3.3), we extend the use of Equation 7 to evaluate the in-cloud and environment contributions to $\left(\overline{w'CO_2'}\right)$ at all model levels. Thereby, we still keep the 2D $a_{c,w}$ as the projected cloud cover to define in-cloud and environment columns over the DALES grid. Inserting this decomposition into the vertically resolved CO_2 budget Equation 2 then allows diagnosing their contributions to $\overline{CO_2}(z)$.

Finally, to assess whether shallow convective clouds and clear air entrainment play a role in organizing the transport of key variables in the rainforest-cloud system as represented in Figure 1 (Section 3.4) we partition the horizontally averaged covariance between H_2O (specific humidity, q) and CO_2 $\left(\left(\overline{q'CO_2'}\right)\right)$ into in-cloud and environment contributions (Equation 12).

$$\left(\overline{q'CO_2'}\right) = a_{c,w}\left(\overline{q'CO_2'}^{cl}\right) + (1 - a_{c,w})\left(\overline{q'CO_2'}^{env}\right) \tag{12}$$

Using Equation 12, we also calculate the partitioned horizontally averaged correlation factor (r) by scaling $\left(\overline{q'CO_2'}\right)$ by the horizontal variation in q (σ_q) and CO_2 (σ_{CO_2}) (Equation 13).

$$r = \frac{a_{c,w}\left(\overline{q'CO_2'}^{cl}\right) + (1 - a_{c,w})\left(\overline{q'CO_2'}^{env}\right)}{\sigma_q\sigma_{CO_2}} \tag{13}$$

3. Results

3.1. Model Evaluation

We begin by evaluating the DALES simulation with the CloudRoots-Amazon22 observations, focusing on the most relevant measured quantities that affect the simulated energy, water, and carbon cycles above the rainforest: the surface energy balance, $\left(\overline{w'CO_2'}\right)_s$, clear-to-cloudy boundary layer (z_i), and cloud layer development, and the evolution of the vertical structure of specific humidity (q), potential temperature (θ) and atmospheric CO_2.

3.1.1. Model Versus Observations: Surface Fluxes and Cloud Development

The simulated and observed diurnal evolution of the surface fluxes of sensible (H) and latent (LE) heat (Figure 2a) of the 6-day aggregate at 10 m above the canopy top ($z = 50$ m) are similar, although DALES tends to slightly overestimate both (Root Mean Square Error (RMSE—LE: 66.76 W m^{-2}, H: 19.07 W m^{-2}), largely consistent with the net radiation available (Figure S1 in Supporting Information S1). Both observations and simulation suggest that the magnitude of LE is almost double the magnitude of H, characteristic for rainforest conditions with a high moisture content (e.g., von Randow et al., 2004).

Similar to H and LE, DALES effectively simulates the diurnal cycle of $\left(\overline{w'CO_2'}\right)_s$ (Figure 2b) (RMSE of 5.45 μmol m^{-2} s^{-1}), with a clear photosynthesis signal but with some shifts in the minimum values throughout the day. Throughout the day, the rainforest has an uptake of 10–20 μmol m^{-2} s^{-1} (≈18–36 ppm h^{-1} uptake throughout the canopy ($z = 50$ m) in standard atmospheric conditions $T_0 = 25$°C and $p_0 = 1{,}013.25$ hPa). A notable difference is the observed near-zero flux during the morning transition (6–8 LT), which is not represented within DALES. González-Armas et al. (2025), who investigated the in-canopy fluxes observed during CloudRoots-Amazon22, suggests that there is a complex flux divergence profile within the canopy that our single-layer, bulk canopy surface model does not appropriately account for. This flux divergence results from a combination of the flush-up of stored CO_2 within the canopy, the initiation of photosynthesis at the canopy top, and ongoing respiration at the canopy bottom, as the subcanopy remains decoupled from the upper canopy and atmosphere (Dupont et al., 2024). Combined, these features offset the measured flux, resulting in a net zero flux as observed during the morning transition. Missing these features in the bulk canopy representation may explain why DALES cannot produce a near zero-flux during the morning transition. Fortunately, after 8 LT, once the model has spun-up and the morning transition has finished, the simulated $\left(\overline{w'CO_2'}\right)_s$ becomes more realistic. Hence, we can focus our analysis after this time step.

The development of z_i, clouds and cloud layer (Figure 2c) are also accurately represented by DALES (RMSE z_i of 75.63 m) and in accordance to previous research (Giangrande et al., 2020; Henkes et al., 2021; Vilà-Guerau de Arellano et al., 2020). After a stable early morning, z_i grows rapidly by 150–200 m h^{-1}. After 10 LT, active shallow convective clouds form as a_c, $a_{c,w}$ and a_{cc} increase (Figure 2d), peaking at 0.30, 0.23, and 0.16 at 14 LT, respectively. The formed clouds have a base around 1.5 km, with a horizontal and vertical extent of respectively 500 m and 0.5–2 km, in both model and observations. After 14 LT, clouds decrease in activity and gradually dissipate toward a nearly cloud-free dusk. The evolution of the cloud layer top, and consequently the vertical extent to which the clouds can influence the vertical distribution of CO_2, follows the expected linear time-scaling with surface buoyancy flux (Stevens, 2007).

3.1.2. Model Versus Observations: Vertical Structure of the Lower Troposphere

In the vertical, DALES successfully captures θ, q and CO_2 in the lower tropical troposphere at 12 and 13 LT (Figures 3a–3c, vertical profiles at 6, 9, 12, 15, and 18 LT are included in Figure S2 in Supporting Information S1). For θ, a well-mixed layer is clearly present in the lowest 1.5 km. The model and observations align well, with a RMSE of 0.45 K. Similar to θ, q is observed to be relatively well-mixed below 1,200 m. However, the LES overestimates this well-mixedness somewhat, yielding a RMSE of 1.12 g kg^{-1}. Similar to θ and q, DALES successfully captures the vertical structure of CO_2 (RMSE: 0.94 ppm), with a small inversion around 1,200 m at 13 LT.

The 6-day aggregated tower observations of the CO_2 mole fractions at 24, 38, 53, 79, and 321 m reflect the aforementioned (Section 2.2) flush-up signal after sunrise (Culf et al., 1997; Dupont et al., 2024; González-Armas et al., 2025) (Figure 3d). These observations show that the relatively high CO_2 mole fractions near the surface (24 m) decrease rapidly, whereas mole fractions higher up the tower (38–79 m) increase at a similar rate. At 53 m, which is ∼13 m above the canopy, CO_2 mole fractions remain relatively constant before 10 LT, reflecting a well-mixed value composed of the values from in-canopy air with the residual layer above. The CO_2 mole fraction at 321 m, the furthest observation away from the canopy and thus not directly influenced by the rainforest processes, approaches this mixed-layer value just before 10 LT, two to three hours after the lowest 80 m of the atmosphere. The moment at which the 321 m level reaches this well-mixed value coincides with the effective onset of shallow convective clouds and a marked increase in photosynthesis (Figure 2b), followed by a ∼20 ppm reduction toward the mid-afternoon.

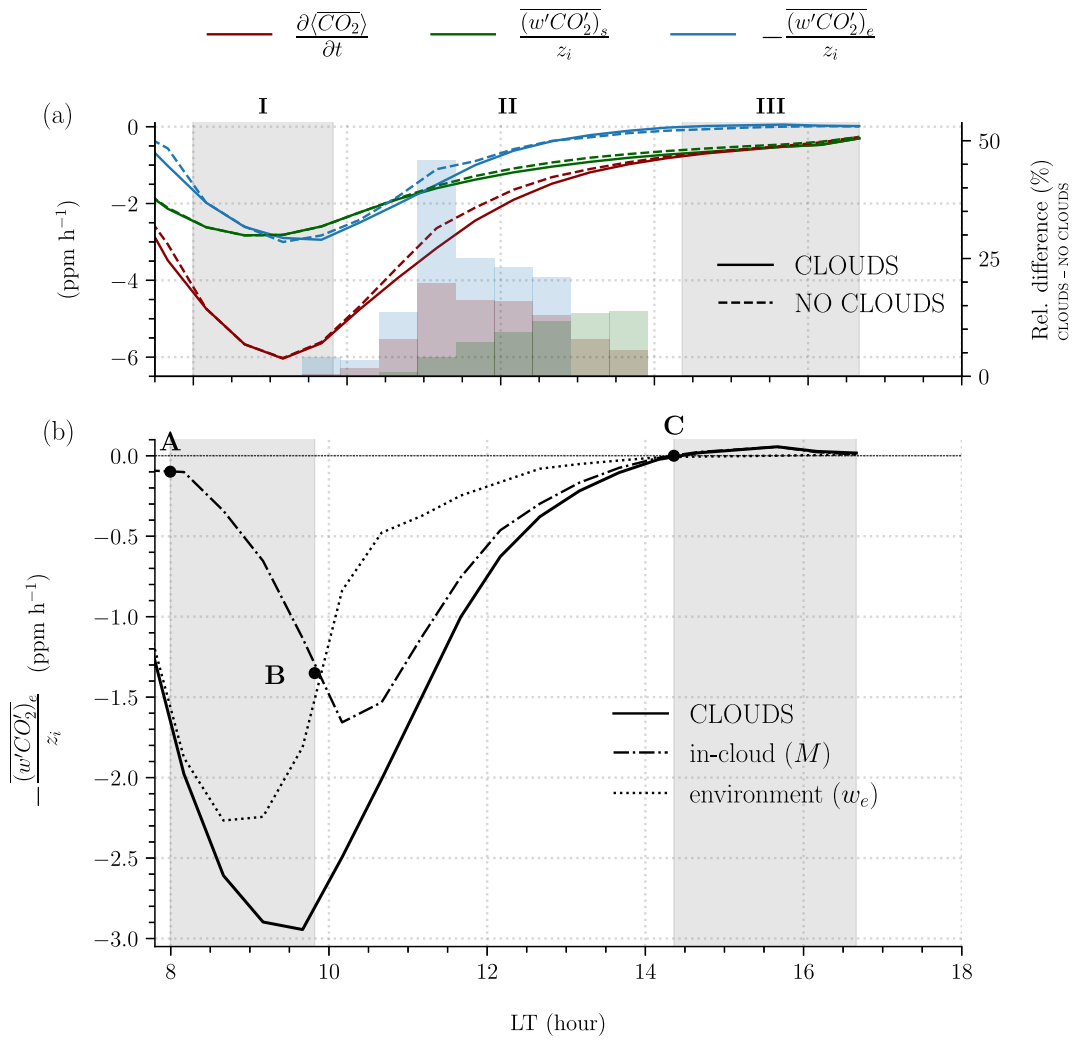

Figure 4. Atmospheric CO_2 budget in the clear-to-cloudy boundary layer (Equation 3) for (a) the CLOUDS (solid line) and NO CLOUDS (dashed line) simulation between 6 and 18 LT, along with the relative difference (%, represented as bars) between the two simulations ((CLOUDS − NO CLOUDS)/NO CLOUDS), relative to the NO CLOUDS simulation. Additionally, (b) shows the in-cloud (dashed dotted line) and environment (dotted line) contributions (Equation 7) to $\left(\overline{w'CO_2'}\right)_e$ of the CLOUDS simulation. The numbers I through III and shading denote the three regimes that can be distinguished from left to right: entrainment-diluting regime (I), cloud-ventilation-and-entrainment regime (II) and the CO_2-assimilation regime (III). Markers A through E denote key time steps aiding in the description of the diurnal cycle of both simulations.

Since the 321 m observations represent the well-mixed layer value following the morning flush-up, we can use this height to assess whether DALES, which we constrained manually to match near-canopy observations (53 m) (Section 2.2), accurately simulates these mole fractions over time. Figure 3d illustrates that DALES effectively captures these mole fractions of CO_2 at 321 m from 8 LT onward, with a closer fit after 10 LT (RMSE CO_2 after 8 LT: 4.723 ppm, after 10 LT: 1.995 ppm), allowing us to assess the CO_2 budget from these times onward.

3.2. Clear-to-Cloudy Boundary Layer CO_2 Budget

To quantify the contributions from in-cloud venting and clear air entrainment alongside rainforest CO_2-assimilation on the clear-to-cloudy boundary layer CO_2 mole fractions, we present the total tendency for the CLOUDS and NO CLOUDS simulations, and these contributions to the total tendency of the CLOUDS simulation, throughout the day (Equation 7) in, respectively, Figures 4a and 4b. Moreover, we present the relative difference (%) between the CLOUDS and NO CLOUDS simulation ((CLOUDS − NO CLOUDS)/NO CLOUDS), relative to the NO CLOUDS simulation, in Figure 4a. For our analysis, we break down each flux contribution following Equation 11 in

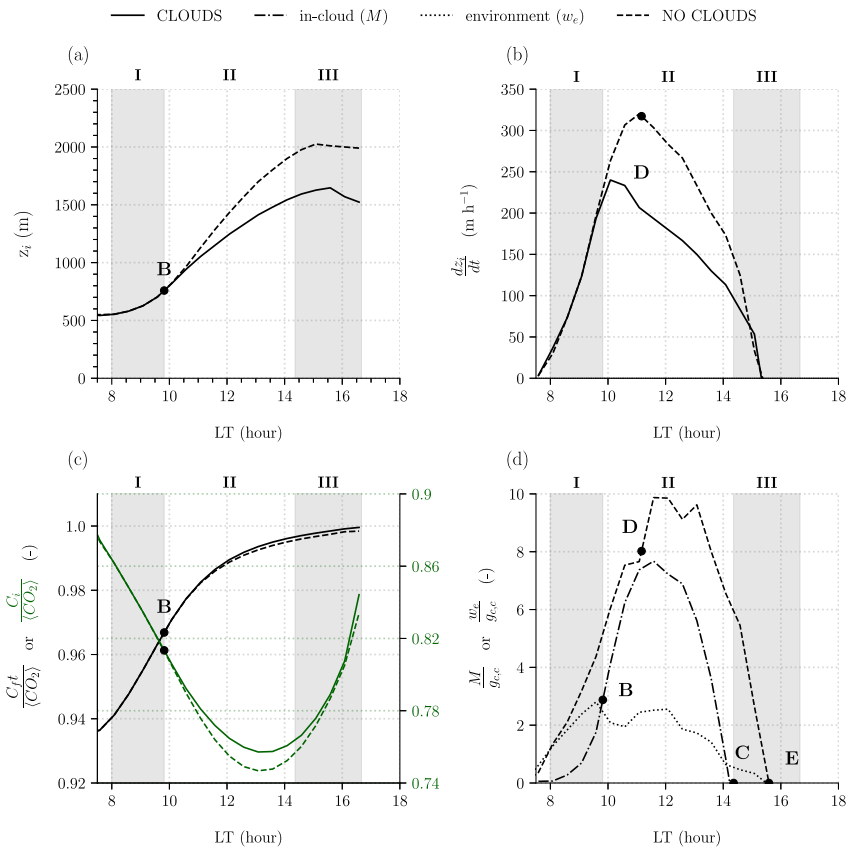

Figure 5. Different terms composing the atmospheric CO_2 budget in the clear-to-cloudy layer from Equation 11: (a) boundary layer height (z_i), (b) growth rate of z_i, (c) ratios between the internal mole fraction (C_i) or free tropospheric mole fraction (C_{ft}) and the clear-to-cloudy boundary layer mole fraction $(\langle CO_2 \rangle)$ of CO_2, and (d) ratios of the characteristic velocities (in-cloud (dashed dotted line) contribution represented by the mass flux (M), the environment (dotted line) contribution and NO CLOUDS (dashed line) simulations represented by the entrainment velocity (w_e), against the stomatal conductance at the rainforest canopy level $(g_{c,c})$. The numbers I through III and shading denote the three regimes that can be distinguished from left to right: entrainment-diluting regime (I), cloud-ventilation-and-entrainment regime (II) and the CO_2-assimilation regime (III). Markers A through E denote key time steps aiding in the description of the diurnal cycle of both simulations.

Figure 5. More specifically, we present the development and growth rate of z_i (Figures 5a and 5b), the ratio between the clear-to-cloudy boundary layer and the cloud layer $\left(\frac{C_{ft}}{\langle CO_2 \rangle}\right)$ or internal CO_2 mole fractions $\left(\frac{C_i}{\langle CO_2 \rangle}\right)$ resembling ΔC_{atm} and $\Delta C_{vegetation}$ (Figure 5c), and the ratios of the characteristic velocities (M and w_e against $g_{c,c}$) (Figure 5d) in time. The markers A through E in both figures denote key time steps aiding in the description of the diurnal cycle of both simulations. In the following, we first concentrate on analyzing the CLOUDS simulation (solid lines) (Section 3.2.1), before assessing the differences with the budget in the NO CLOUDS simulation (Section 3.2.2).

3.2.1. With Clouds: Joint Regime of Cloud Ventilation and Entrainment

Throughout the day, CO_2 is ventilated and mixed at a rate $\left(\frac{\partial \langle \overline{CO_2} \rangle}{\partial t}\right)$ of 2–6 ppm h^{-1}, diluting the clear-to-cloudy boundary layer in CO_2 (Figure 4a). Although both $\left(\overline{w'CO_2'}\right)_s$ and $\left(\overline{w'CO_2'}\right)_e$ contribute to this dilution, the latter outweighs the former before 14:21 LT, establishing an atmospheric-dilution regime and CO_2-assimilation regime, respectively, in accordance to previous research (Davis et al., 1997; Faassen et al., 2025; Huang et al., 2011; Verzijlbergh et al., 2009; Vilà-Guerau de Arellano et al., 2004). However, partitioning $\left(\overline{w'CO_2'}\right)_e$ between in-cloud (dash-dotted lines) and environment (dotted lines) contributions according to Equation 7 reveal that with the presence of clouds, $\left(\overline{w'CO_2'}\right)_e$ shifts from being dominated by clear air entrainment before 9:49 LT,

to having a joint contribution between in-cloud venting and clear air entrainment under increasing cloud fraction. As a result, we can separate the atmospheric-dilution into two separate regimes: an "entrainment-diluting regime" before 9:49 LT, and the "cloud-ventilation-and-entrainment regime" between 9:49 and 14:21 LT (previously hinted to by Faassen et al. (2025) and Verzijlbergh et al. (2009)).

The onset of the entrainment-diluting regime occurs after model initialization, flush-up and start of dry convection at 8 LT (marker A). At this time, a growing entrainment velocity w_e (Figure 5d) rapidly grows the boundary layer (markers A to B). The combined effect on the $\langle CO_2 \rangle$ budget (term 4 in Equation 11) reduces $\langle CO_2 \rangle$ at a rate of -3 ppm h^{-1}, contributing roughly half the $\langle CO_2 \rangle$ sink. The effectiveness of this entrainment-dilution is limited both by the growing z_i, and by the dilution itself, which brings $\langle CO_2 \rangle$ toward C_{ft}. As a result, the ratio between these mole fractions ($\frac{C_{cl}}{\langle CO_2 \rangle}$, Figure 5c) approaches a value of one (0.985). Approximately 2 hours later (09:49 LT), following the formation of more actively buoyant shallow convective clouds (Figure 2d), the cloud-ventilation-and-entrainment regime commences (marker B). At this time, the contribution of in-cloud ventilation (term 3 in Equation 11) increases rapidly, whereas that of w_e (term 4) gradually decreases (Figure 5d).

At 14:21 LT, approximately 4 hr and 30 min after the onset of moist convection, $\left(\overline{w'CO_2'}\right)_e$ ceases as the lower troposphere reaches well-mixed conditions ($\frac{C_{ft}}{\langle CO_2 \rangle} > 0.995$, marker C). At this moment, the third and last regime, the CO_2-assimilation regime, commences as rainforest CO_2-assimilation (term 2 in Equation 11) becomes the sole controlling factor of the CO_2 budget of the boundary layer. Apart from the CO_2-assimilation regime, photosynthesis is an active sink of CO_2 throughout the entire diurnal cycle. Assimilation of CO_2 has a similar magnitude as $\left(\overline{w'CO_2'}\right)_e$, despite the fact that the canopy-scale conductance is significantly smaller than the mass flux and entrainment velocities (M and w_e being 2 to 8 times larger, as shown in Figure 5d). The effectiveness of the CO_2-assimilation by the vegetation is primarily governed by the fact that the gradient in CO_2 for the vegetation ($\Delta C_{vegetation}$) is far greater than that between the boundary layer and free troposphere (ΔC_{atm}). The vegetation actively uses C_i for photosynthesis, reducing $\frac{C_i}{\langle CO_2 \rangle}$ until midday while maintaining CO_2 uptake as the boundary layer CO_2 mole fraction decreases. Near 13 LT, the internal mole fraction of CO_2 for the vegetation is lowered to ~25% the well-mixed boundary layer value. This behavior is in accordance with observations and detailed analysis presented by González-Armas et al. (2025).

Overall, throughout the entire day, the clear-to-cloudy boundary layer CO_2 budget is controlled by an interplay between in-cloud ventilation (~23%), clear air entrainment (~21%), next to continued rainforest CO_2-assimilation (~56%), with their relative importance varying per diurnal regime.

3.2.2. Without Clouds: Entrainment Becomes the Governing Process

When latent heating is prevented from influencing buoyancy (`NO CLOUDS`, dashed lines), only two regimes remain: the entrainment-diluting and the CO_2-assimilation regime. However, the overall effect on $\frac{\partial \langle \overline{CO_2} \rangle}{\partial t}$ appears visually minimal (Figure 4a). An examination of the different terms comprising the atmospheric CO_2 budget in the clear-to-cloudy layer, as expressed in Equation 11, shows that the difference between the two simulations is primarily governed by subtle compensating effects between M, z_i, and w_e, which we shall discuss in more detail below.

Within the `NO CLOUDS` simulation, M is forced to zero as clouds are considered passive. As a consequence, cloud ventilation (term 3 in Equation 11) is lost. If the missing cloud ventilation is treated individually, no ventilation by mass fluxes should yield a relative accumulation of $\langle CO_2 \rangle$ compared to the `CLOUDS` simulation. However, a striking observation is that without clouds, increasing w_e (term 4 in Equation 11) compensates for the missing cloud ventilation.

Next to the missing M, z_i becomes up to 500 m larger for the `NO CLOUDS` simulation compared to the `CLOUDS` simulation, comparable to Vilà-Guerau de Arellano et al. (2005). Shallow convective clouds act as valves which evacuate mass from the subcloud layer (e.g., Nicholls & Lemone, 1980; van Stratum et al., 2014; Verzijlbergh et al., 2009). As a result of this mass removal, z_i grows about 150 m h^{-1} slower in the `CLOUDS` simulation compared to the `NO CLOUDS` simulation once active buoyant clouds form around 10 LT (marker B). The effects of the larger z_i is twofold. On the one hand, the increasing z_i causes $\langle CO_2 \rangle$ to be diluted across a larger volume, reducing the overall CO_2 mole fraction. On the other hand, the increasing volume reduces the entrainment-

dilution in the NO CLOUDS simulation as every entrained CO_2-dilute parcel must be mixed into a deeper layer to lower $\langle CO_2 \rangle$. If the effects of the growing z_i would be treated individually, an increasing z_i should lead to a lower $\langle CO_2 \rangle$ when clouds are passive. However, similar to M, the effects are strikingly compensated by the increase in w_e in the NO CLOUDS simulation.

A possible explanation of the increased w_e can be found in the radiation and energy balance, as the rainforest canopy top receives 55 W m^{-2} more net radiation under clear sky conditions. Consequently, the sensible heat flux is increased by 32 W m^{-2} and the development of large, strong turbulent structures is promoted, increasing w_e. Moreover, since more grid columns are considered as "clear", the relative contribution from the environment and thus w_e in Equation 11 increases. It is worth noting that w_e peaks around midday after a fast increase at 11 LT (marker D in Figure 5c).

The increase in w_e is the primary process responsible for yielding an approximately similar NO CLOUDS and CLOUDS simulation throughout the day. However, quantifying the relative difference between the CLOUDS and NO CLOUDS simulations, relative to the NO CLOUDS simulation, reveals a substantial discrepancy between 10 and 14 LT. During this period, the total tendency in the CLOUDS simulation is approximately 20%–25% greater (Figure 4a). The largest contribution to this discrepancy arises from $\left(\overline{w'CO_2'}\right)_e$, which is more than 25% greater in the CLOUDS simulation following the onset of shallow convective clouds. Although the increasing w_e and z_i in the NO CLOUDS simulation compensate to some extent for the absence of M, the relative difference highlights that the net removal by $\left(\overline{w'CO_2'}\right)_e$ in the NO CLOUDS simulation is 20%–25% less effective than when clouds are present. As a result, the NO CLOUDS simulation reaches well-mixed conditions approximately an hour later, at 15:35 LT (marker E). Additionally, the rainforest vegetation must lower its C_i to adjust to the slightly higher $\langle CO_2 \rangle$ between 10 and 14 LT (Figure 5c).

3.3. Vertically Resolved CO_2 Budget: Shallow Convective Clouds Raise Vertical CO_2 Levels Up to Double z_i

The CLOUDS and NO CLOUDS simulations differ more substantially above z_i during the cloud-ventilation-and-entrainment regime (Figure 6). Before this time, at 9 LT (Figure 6a), the vertically resolved CO_2 budget follows a clear entrainment profile: dry convective thermals transport CO_2 from the canopy and boundary layer (net divergence of 8 ppm h^{-1}) to a shallow layer around z_i (between z_i to $1.3z_i$), where CO_2 is deposited (net convergence of 16 ppm h^{-1}). At the same time, CO_2-assimilation by the rainforest actively removes CO_2, explaining the negative CO_2 tendency down to the lowest model level.

At midday (Figure 6b), the entrainment signal as observed at 9 LT, tough in smaller magnitude (2.5 ppm h^{-1}), remains for the NO CLOUDS simulation. For the CLOUDS simulation, the convergence signal of entrainment is spread up to $2.5z_i$, following the linear time-scaling with surface buoyancy flux (Stevens, 2007). The signal has a characteristic bell-shaped distribution (Ouwersloot et al., 2013; Verzijlbergh et al., 2009; Vilà-Guerau de Arellano et al., 2005), with the largest convergence of CO_2 with a rate up to 2 ppm h^{-1} at the bottom of the cloud layer, and decreasing values with height. Flux partitioning into actively buoyant in-cloud and environment grid columns according to Equation 7 (Figure 6e), reveal that this bell-shaped convergence signal can be primarily attributed to cloudy grid columns.

The vertical distribution of CO_2 results from an interplay between entrainment from the boundary layer and in-cloud ventilation. Starting at the surface, dry turbulence in clear air (environment grid columns) transports CO_2 upward (divergence of 2 ppm h^{-1}). At z_i, the transported CO_2 is deposited (convergence of 2 ppm h^{-1}), but this is balanced by a net divergence of slightly more than 2 ppm h^{-1} in the in-cloud grid columns. That is, during the cloud-ventilation-and-entrainment regime, primarily dry convective thermals bring CO_2 from the subcloud layer to z_i, whereas at z_i, moist convective thermals pick up this CO_2 and transport it to higher vertical levels within the cloud layer, increasing CO_2 mole fractions up to $2.5z_i$.

Toward the end of the afternoon during the CO_2-assimilation regime (Figures 6c and 6f), the signals from both simulations weaken as the lower troposphere reaches a well-mixed state. As a result, there is minimal to no net vertical displacement of CO_2 within the lower troposphere. Without clear convergence at z_i, the remaining CO_2 divergence within the boundary layer can be primarily attributed to continued CO_2-assimilation. However, since

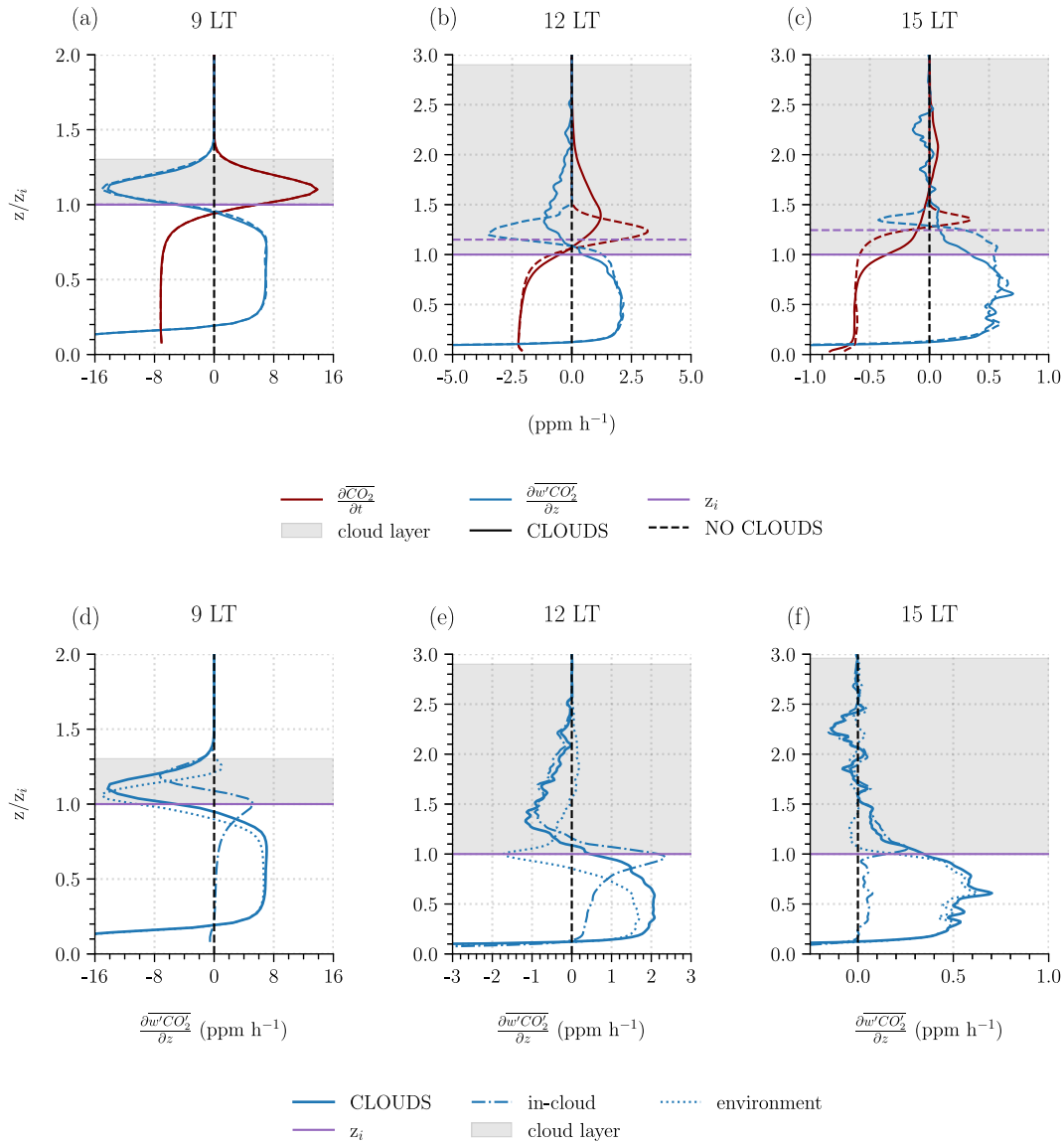

Figure 6. Vertically resolved budget of atmospheric CO_2 for the NO CLOUDS and CLOUDS (solid line) simulations (a–c), split into in-cloud (dashed dotted line) and environment (dotted line) contributions (d, e), at three time steps: (a, b) 9 LT, (b, e) 12 LT and (c, f) 15 LT.

the cloud fraction is still larger than zero (Figure 2d), a weak (0.2 ppm h^{-1}) cloud ventilation signal remains visible, transporting CO_2 upward and primarily mixing the atmosphere >2.5z_i.

3.4. Shallow Convective Clouds Organize the Vertical Correlation Pattern Between CO_2 and H_2O

The preceding analysis of the contributions to the boundary layer (Section 3.2) and the vertically resolved CO_2 budget (Section 3.3) highlight the important role of shallow convective clouds in shaping these budgets. The associated mixing and vertical transport processes point to a pronounced coupling between the rainforest surface and the upper atmosphere (extending up to 2.5z_i), regulated by these clouds. The presence of such coupling reflects the observed transition from a negative to positive CO_2-H_2O correlation with height as shown in Figure 1. To determine the extent to which shallow convective clouds shape this coupling, we proceed to analyze the CO_2-H_2O correlation signal and the horizontally averaged correlation coefficient (r) between fluctuations of H_2O and CO_2 at z_L, z_M, and z_H at 13 LT in DALES. We compare the NO CLOUDS simulation with the in-cloud and environmental contributions of the CLOUDS simulation (together they represent the CLOUDS signal), alongside

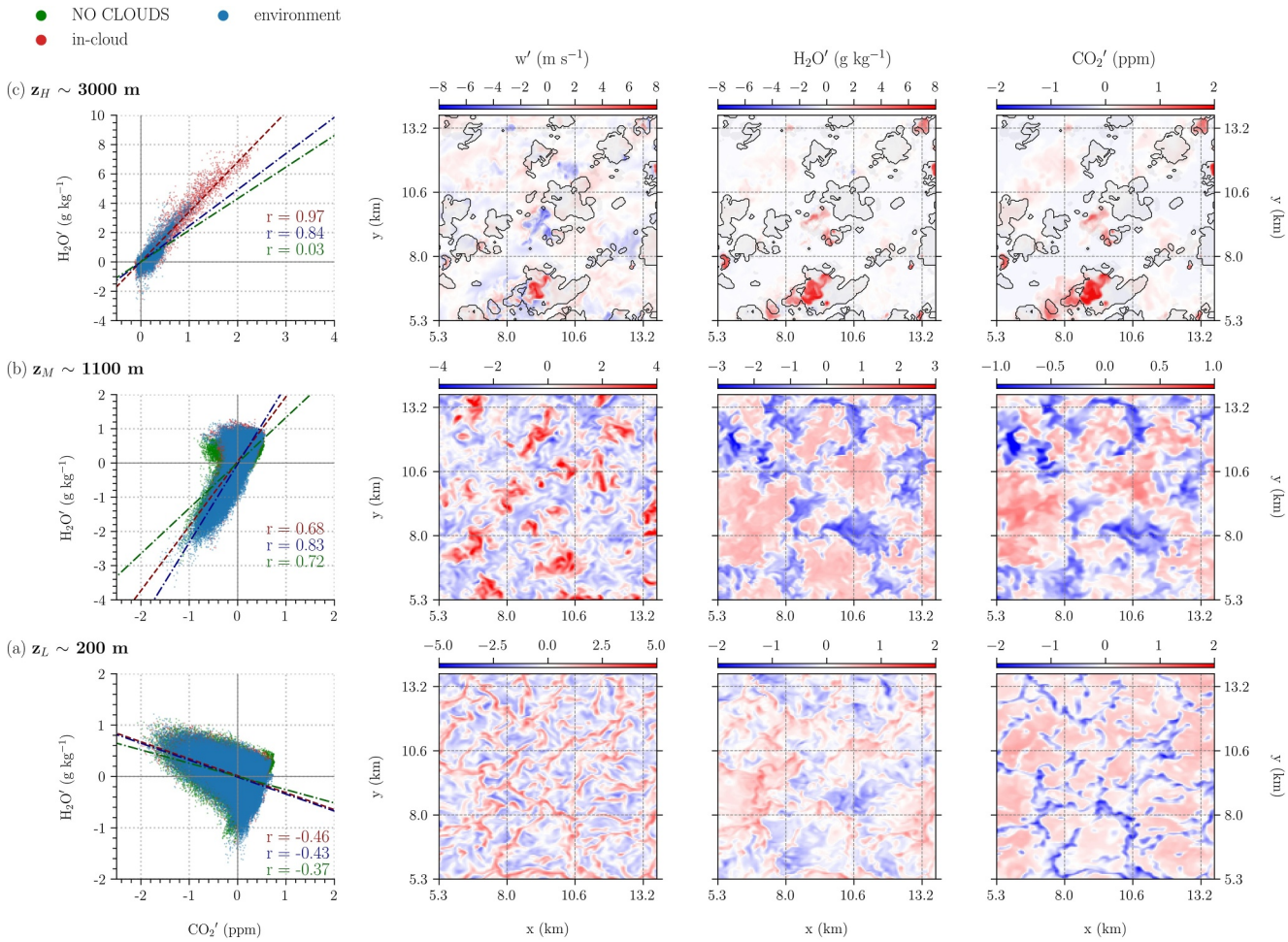

Figure 7. Horizontal instantaneous CO_2-H_2O correlation signal and the horizontally averaged correlation coefficient (r) in DALES at 13 LT between fluctuations of H_2O and CO_2 for the NO CLOUDS and in-cloud and environmental contributions of the CLOUDS simulation (together they represent the CLOUDS signal) (left column), alongside the instantaneous horizontal (x, y) cross section of fluctuations (φ') in H_2O, CO_2 and vertical velocity (w) around spatial domain-averages ($\overline{\varphi}$) in the CLOUDS simulation with the upward-moving cloud average boundaries colored in black contours ($a_{c,w}$) (right columns). Represented at z_L ((a), roughness sublayer ∼200 m), z_M ((b), subcloud layer ∼1,100 m), z_H ((c), cloud layer at ∼3,000 m) similar to Figure 1. Simulated mean cloud-average cloud fraction (a_c), upward-moving cloud-average cloud fraction ($a_{c,w}$) and core-average cloud fraction (a_{cc}) are approximately: 0.28, 0.21, and 0.14, respectively.

the instantaneous horizontal (x, y) cross section of the CLOUDS simulation with the upward-moving cloud average boundaries ($a_{c,w}$) in Figure 7. The instantaneous cross section represents a spatial representation of H_2O' and CO_2', similar to the flight tracks as shown Figure 1. Benefiting from the LES simulation, we can also assess the fluctuations in w to get the full picture. In the following, we first examine the CLOUDS simulation, before comparing it with the NO CLOUDS simulation. We thereby assess the vertical aspects prior to considering the temporal aspects.

The correlation figures and horizontally averaged r-values of DALES at 13 LT reflect the negative to positively correlated pattern with height, similar to Figure 1. However, in contrast to the observations, the positive correlation is already clearly defined at z_M, rather than solely at z_H. This difference may be attributed to minor discrepancies between the DALES simulation and the observations, as discussed in Section 3.1. Additionally, the absence of surface heterogeneity from the Amazon rainforest within DALES, which is captured by the aircraft observations, may also contribute to this difference. As a result, we focus on comparing the processes occurring at the roughness sublayer (z_L) and cloud layer (z_H).

At z_L (Figure 7a), the strong negative correlation ($r \approx -0.5$) can be attributed to the mixing of CO_2-diluted air from photosynthesis and moisture-rich air from evapotranspiration by the rainforest in upward moving thermals, which is in accordance to previous research (Dupont et al., 2024; Vilà-Guerau de Arellano et al., 2004) and

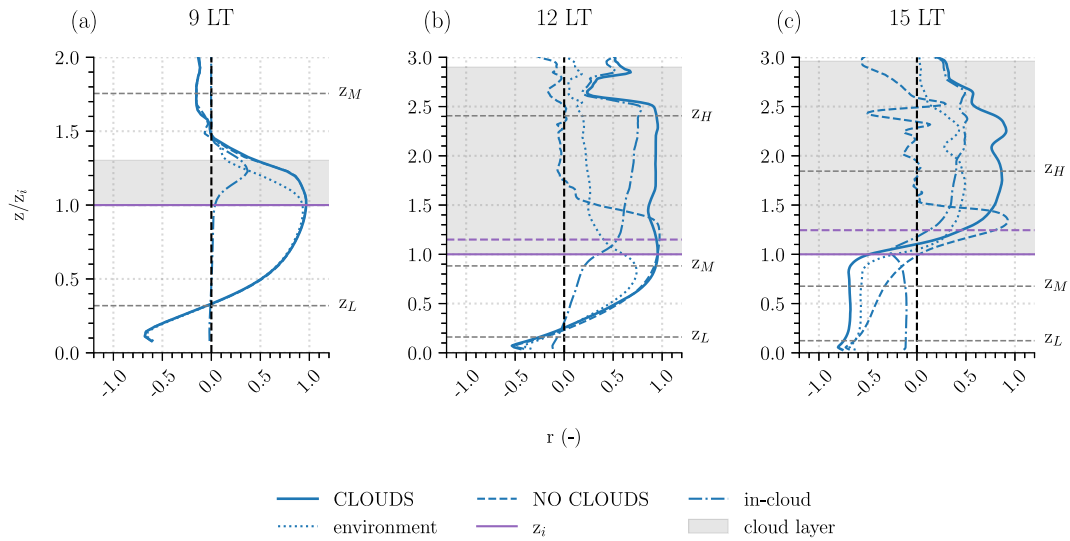

Figure 8. Vertical profiles of the horizontally averaged correlation coefficient (r) between CO_2 and H_2O for the CLOUDS (solid line), split into in-cloud (dashed dotted line) and environment (dotted line) contributions, at three time steps: (a) 9 LT, (b) 12 LT and (c) 15 LT. Vertical lines highlight the heights of z_L (roughness sublayer at ∼200 m), z_M (subcloud layer at ∼1,100 m) and z_H (cloud layer at ∼3,000 m) similar to Figure 1.

observations from Figure 1. At z_H (Figure 7c), the strong positive correlation ($r \approx 1$) can be attributed to an interplay of in-cloud ventilation and the environment (Jonker et al., 2008; Ouwersloot et al., 2013; Verzijlbergh et al., 2009). This interplay is twofold. On the one hand, convective thermals originating at the surface, carrying bulk boundary-layer moisture and CO_2, possess an excess of both CO_2 and moisture compared to decreasing ambient values with height. This excess in CO_2 and H_2O is jointly transported upward, reflecting the positive correlation. In dry thermals, both CO_2 and H_2O are deposited close to z_i, whereas in cloudy thermals CO_2 and H_2O are transported up to $2.5z_i$. Figure 7c shows that clouds actively organize this vertical transport, with r increasing by 0.13 in the in-cloud columns. Conversely, in the environment, compensating descending motions from the free troposphere, characterized by reduced CO_2 and moisture from the free troposphere, entrain into the boundary layer. Consequently, these motions also give rise to a positive correlation.

The spatial representation of w', H_2O' and CO_2' reveal that the vertical exchange of CO_2 at z_H is confined to cloud scales of <2 km. Within these dynamic clouds, strong updraughts (w' up to 9 m s^{-1}) bring air with bulk-boundary layer moisture and CO_2 mole fractions upward (ϕ' up to 3–6 ppm or g kg^{-1}). Depending on the core updraught strength, CO_2 and H_2O are displaced laterally at the cloud base, halfway the cloud layer or at the cloud top. These cloud scales typically fall within the "gray zone" at which convection in numerical weather prediction and climatological models can be represented (Honnert et al., 2020; Pedruzo-Bagazgoitia et al., 2019; Tomassini et al., 2023), making it a challenge to accurately account for these processes in estimates of the diurnal CO_2 budget.

Without clouds, the turbulent thermals at z_L grow and decrease in magnitude (Dupont et al., 2024; Hooft et al., 2019), eventually vanishing above the raised z_i, resulting in $r = 0$ at z_H. These thermals detrain their CO_2 and moisture in a layer between z_i and $1.3z_i$ and cannot transport CO_2' and H_2O' to z_H, as discussed in Section 3.3. These findings confirm that shallow convective clouds are responsible for extending the positive CO_2-H_2O correlation above z_i, as the correlated patterns remain consistent throughout the boundary layer for the CLOUDS and NO CLOUDS simulation at z_L and z_M (Figures 7b and 7c).

Over the course of the day, from 9 to 15 LT (Figure 8), the CO_2-H_2O correlation pattern with height remains a distinct structure. At both 9 and 12 LT, the positive correlation in the NO CLOUDS simulation extends up to the top of the entrainment zone (up to $1.5z_i$), whereas in the CLOUDS simulation, the positive r extends up to $2.5z_i$ and is primarily attributed by cloudy grid columns. By 15 LT, the correlation is primarily organized by fluctuations in H_2O since the boundary layer becomes well-mixed in CO_2. For H_2O, a strong and progressively more pronounced inversion develops over the course of the day, shaped by the relatively dry free troposphere above and the

replenishment of moisture through evapotranspiration over the rainforest. Consequently, entrainment from the boundary layer and in-cloud ventilation primarily transports moist air upward and drier air downwards. It is worth noting that this transport is sufficiently strong that a positive correlation above z_i can still be observed.

4. Conclusions

In this study, we investigated the turbulent exchange of CO_2 in the lower troposphere above the Amazon rainforest across clear boundary layers that become cloudy due to the formation of shallow convective clouds throughout the day. Specifically, we examined the interactions between clear air entrainment (dry convection), in-cloud ventilation (moist convection), next to rainforest CO_2-assimilation. Furthermore, we examined whether shallow convective clouds organize the vertical CO_2 exchange within the lower tropical troposphere, as illustrated in Figure 1. We constructed and validated a representative DALES simulation of a shallow convective day above the Amazon rainforest using the CloudRoots-Amazon22 campaign observations. Two simulations were run: one without and one with clouds, where we partitioned the latter into its respective in-cloud and environmental contributions to the clear-to-cloudy boundary layer and vertically resolved CO_2 budget. Our results demonstrated that the interplay between clear air entrainment, in-cloud ventilation by shallow convective clouds and CO_2-assimilation is essential to describe the diurnal and vertical distribution of CO_2 within the lower tropical troposphere.

In the diurnal cycle, the clear-to-cloudy transition allows the formulation of three distinct diurnal regimes depending on the main governing process: entrainment-diluting regime, cloud-ventilation-and-entrainment regime and the CO_2-assimilation regime. Shallow convective clouds (~23%), clear air entrainment (~21%), and rainforest CO_2-assimilation (~56%) collectively shape the clear-to-cloudy boundary layer CO_2 budget, with their relative importance varying per diurnal regime. Without dynamically active shallow convective clouds, cloud ventilation is absent, and a stronger entrainment alone governs the diurnal evolution and vertical distribution of CO_2 within the boundary layer. Since mass removal by clouds is suppressed, the boundary layer can deepen by up to 500 m relative to cloudy conditions. These compensating effects therefore result in a total CO_2-flux convergence comparable to a cloudy boundary layer. Nonetheless, entrainment and CO_2-assimilation alone are 20%–25% less effective in mixing CO_2 in the boundary layer, causing the boundary layer to become well-mixed up to an hour later compared to cloudy conditions.

In the vertical, shallow convective clouds actively couple the rainforest surface to the upper atmosphere. Cloud ventilation and entrainment collectively facilitate the vertical exchange of CO_2 up to heights twice the boundary layer depth and at a rate comparable to CO_2-assimilation at the rainforest canopy, significantly affecting its vertical distribution until late afternoon. The clouds organize the turbulent exchange of CO_2 by extending the positive end of the negative-to-positive CO_2-H_2O correlation from the boundary layer top upward. Spatial analysis revealed that this turbulent exchange is predominantly confined to cloud scales of <2 km. Within these dynamic clouds, strong updraughts (fluctuations of vertical velocity up to 9 m s^{-1}) transport CO_2 and moisture from the boundary layer upward. These cloud driven processes fall within the gray zone of resolving convection, posing a challenge for accurate representation in numerical weather prediction and climatological models. Over time, the vertical negative to positively correlated signal persists, shifting to being primarily driven by fluctuations in H_2O when the lower troposphere becomes well-mixed in CO_2.

Although our study is constrained by the available observations, we believe it offers significant insights into the interactions between rainforest CO_2-assimilation, clear air entrainment, and in-cloud ventilation by shallow mass fluxes, as well as the organization of turbulent CO_2 exchange by shallow convective clouds in the lower tropical troposphere. Future research should prioritize assessing the impact of potential misrepresentations of these clear-to-shallow convective processes in numerical weather prediction and climate models, such as the Integrated Forecasting System (IFS) of the European Centre for Medium-Range Weather Forecasts, which underpin most inverse-modeled CO_2 budget estimates. Greater complexity should also be incorporated by examining the relative contributions of both local and large-scale processes on the turbulent exchange of CO_2. Example processes are the role of multi-layer canopy dynamics during the morning transition, large-scale advection, subsidence, the role of shallow-to-deep convective clouds and synoptic weather systems. Ongoing work aims to build upon the framework established in this study, employing detailed observations from campaigns such as CloudRoots-Amazon22 alongside LES and the IFS at resolutions of 4.4, 9, and 25 km, to further investigate and resolve these multi-scale dynamics involved in the turbulent exchange of CO_2 over the Amazon and ecosystems alike.

Conflict of Interest

The authors declare no conflicts of interest relevant to this study.

Data Availability Statement

A copy of the used CloudRoots-Amazon22 data, visualization code, and DALES version 4.4 code are available via the 4-TU repository (de Feiter et al., 2025).

Acknowledgments

This work was supported by the CATRINE project (grand agreement 101135000), funded by the European Union. Views and opinions expressed are however those of the author(s) only and do not necessarily reflect those of the European Union or the Commission. Neither the European Union nor the granting authority can be held responsible for them. Additionally, this study was supported by the Amazon Tall Tower Observatory (ATTO), funded by the German Federal Ministry of Education and Research (BMBF, contracts 01LB1001A, and 01LK1602A), the Brazilian Ministry of Science, Technology and Innovation (MCTI/FINEP, contract 01.11.01248.00) and the Max Planck Society (MPG). ATTO is also supported by the Fundação de Amparo à Pesquisa do Estado do Amazonas (FAPEAM), Fundação de Amparo à Pesquisa do Estado de São Paulo (FAPESP), Universidade do Estado do Amazonas (UEA), Instituto Nacional de Pesquisas Amazônia (INPA), Programa de Grande Escala da Biosfera-Atmosfera na Amazônia (LBA) and the SDS/CEUC/RDS-Uatumã. The CloudRoots-Amazon22 campaign was funded by the Dutch Research Council (NWO under the project CloudRoots–Clouds rooted in a heterogeneous biosphere (https://cloudroots.wur.nl/) (Dutch Research Council NWO OCENW.KLEIN.407).

References

Albright, A. L., Bony, S., Stevens, B., & Vogel, R. (2022). Observed subcloud-layer moisture and heat budgets in the trades. *Journal of the Atmospheric Sciences*, *79*(9), 2363–2385. https://doi.org/10.1175/JAS-D-21-0337.1

Alden, C. B., Miller, J. B., Gatti, L. V., Gloor, M. M., Guan, K., Michalak, A. M., et al. (2016). Regional atmospheric CO_2 inversion reveals seasonal and geographic differences in Amazon net biome exchange. *Global Change Biology*, *22*(10), 3427–3443. https://doi.org/10.1111/gcb.13305

Anav, A., Friedlingstein, P., Beer, C., Ciais, P., Harper, A., Jones, C., et al. (2015). Spatiotemporal patterns of terrestrial gross primary production: A review. *Reviews of Geophysics*, *53*(3), 785–818. https://doi.org/10.1002/2015RG000483

Andreae, M. O., Acevedo, O. C., Araùjo, A., Artaxo, P., Barbosa, C. G. G., Barbosa, H. M. J., et al. (2015). The Amazon Tall Tower Observatory (ATTO): Overview of pilot measurements on ecosystem ecology, meteorology, trace gases, and aerosols. *Atmospheric Chemistry and Physics*, *15*(18), 10723–10776. https://doi.org/10.5194/acp-15-10723-2015

Bardakov, R., Krejci, R., Riipinen, I., & Ekman, A. M. L. (2022). The role of convective up- and downdrafts in the transport of trace gases in the Amazon. *Journal of Geophysical Research: Atmospheres*, *127*(18), e2022JD037265. https://doi.org/10.1029/2022JD037265

Bastos, A., O'Sullivan, M., Ciais, P., Makowski, D., Sitch, S., Friedlingstein, P., et al. (2020). Sources of uncertainty in regional and global terrestrial CO_2 exchange estimates. *Global Biogeochemical Cycles*, *34*(2), e2019GB006393. https://doi.org/10.1029/2019GB006393

Betts, A. K., Desjardins, R. L., Macpherson, J. I., & Kelly, R. D. (1990). Boundary-layer heat and moisture budgets from FIFE. *Boundary-Layer Meteorology*, *50*(1), 109–138. https://doi.org/10.1007/BF00120520

Botía, S., Komiya, S., Marshall, J., Koch, T., Gałkowski, M., Lavric, J., et al. (2022). The CO_2 record at the Amazon Tall Tower Observatory: A new opportunity to study processes on seasonal and inter-annual scales. *Global Change Biology*, *28*(2), 588–611. https://doi.org/10.1111/gcb.15905

Culf, A. D., Fisch, G., Malhi, Y., & Nobre, C. A. (1997). The influence of the atmospheric boundary layer on carbon dioxide concentrations over a tropical forest. *Agricultural and Forest Meteorology*, *85*(3), 149–158. https://doi.org/10.1016/S0168-1923(96)02412-4

Davis, K. J., Lenschow, D. H., Oncley, S. P., Kiemle, C., Ehret, G., Giez, A., & Mann, J. (1997). Role of entrainment in surface-atmosphere interactions over the boreal forest. *Journal of Geophysical Research*, *102*(D24), 29219–29230. https://doi.org/10.1029/97JD02236

de Feiter, V. S., Janssens, M., de Haas, S. E., Hartogensis, O., Dias-Junior, C. Q., van Asperen, H., et al. (2025). Code and data repository on "turbulent exchange of CO_2 in the lower tropical troposphere across clear-to-cloudy conditions" [Collection]. *4TU.ResearchData*. https://doi.org/10.4121/A72AA7AE-7FD2-450B-A1C4-1FA093D15438.V1

de Rooy, W. C., Bechtold, P., Fröhlich, K., Hohenegger, C., Jonker, H., Mironov, D., et al. (2013). Entrainment and detrainment in cumulus convection: An overview. *Quarterly Journal of the Royal Meteorological Society*, *139*(670), 1–19. https://doi.org/10.1002/qj.1959

Dupont, S., Irvine, M. R., & Bidot, C. (2024). Morning transition of the coupled vegetation canopy and atmospheric boundary layer turbulence according to the wind intensity. *Journal of the Atmospheric Sciences*, *81*(7), 1225–1249. https://doi.org/10.1175/JAS-D-23-0201.1

Faassen, K. A. P., Armas, R. G., Koren, G., Adnew, G. A., Asperen, H. V., Boer, H. J. D., et al. (2025). Tracing diurnal variations of atmospheric CO_2, O_2 and $^{13}CO_2$ over a tropical and a temperate forest. *ESS Open Archive*. https://doi.org/10.22541/essoar.175371783.36208960/v1

Fitzjarrald, D. R., Moore, K. E., Cabral, O. M. R., Scolar, J., Manzi, A. O., & de Abreu Sá, L. D. (1990). Daytime turbulent exchange between the Amazon forest and the atmosphere. *Journal of Geophysical Research*, *95*(D10), 16825–16838. https://doi.org/10.1029/JD095iD10p16825

Friedlingstein, P., O'Sullivan, M., Jones, M. W., Andrew, R. M., Bakker, D. C. E., Hauck, J., et al. (2023). Global Carbon Budget 2023. *Earth System Science Data*, *15*(12), 5301–5369. https://doi.org/10.5194/essd-15-5301-2023

Garstang, M., & Fitzjarrald, D. R. (1999). Observations of surface to atmosphere interactions in the tropics. *Agricultural and Forest Meteorology*, *116*(3–4), 229–230. https://doi.org/10.1016/S0168-1923(03)00003-0

Gatti, L. V., Gloor, M., Miller, J. B., Doughty, C. E., Malhi, Y., Domingues, L. G., et al. (2014). Drought sensitivity of Amazonian carbon balance revealed by atmospheric measurements. *Nature*, *506*(7486), 76–80. https://doi.org/10.1038/nature12957

Gentine, P., Green, J. K., Guérin, M., Humphrey, V., Seneviratne, S. I., Zhang, Y., & Zhou, S. (2019). Coupling between the terrestrial carbon and water cycles—A review. *Environmental Research Letters*, *14*(8), 083003. https://doi.org/10.1088/1748-9326/ab22d6

Giangrande, S. E., Wang, D., & Mechem, D. B. (2020). Cloud regimes over the Amazon Basin: Perspectives from the GoAmazon2014/5 campaign. *Atmospheric Chemistry and Physics*, *20*(12), 7489–7507. https://doi.org/10.5194/acp-20-7489-2020

González-Armas, R., Rikkers, D., Hartogensis, O., Dias-Júnior, C. Q., Komiya, S., Pugliese, G., et al. (2025). Daytime water and CO_2 exchange within and above the Amazon rainforest. *Agricultural and Forest Meteorology*, *372*, 110621. https://doi.org/10.1016/j.agrformet.2025.110621

Henkes, A., Fisch, G., Machado, L. A. T., & Chaboureau, J.-P. (2021). Morning boundary layer conditions for shallow to deep convective cloud evolution during the dry season in the central Amazon. *Atmospheric Chemistry and Physics*, *21*(17), 13207–13225. https://doi.org/10.5194/acp-21-13207-2021

Heus, T., van Heerwaarden, C. C., Jonker, H. J. J., Pier Siebesma, A., Axelsen, S., van den Dries, K., et al. (2010). Formulation of the Dutch Atmospheric Large-Eddy Simulation (DALES) and overview of its applications. *Geoscientific Model Development*, *3*(2), 415–444. https://doi.org/10.5194/gmd-3-415-2010

Honnert, R., Efstathiou, G. A., Beare, R. J., Ito, J., Lock, A., Neggers, R., et al. (2020). The atmospheric boundary layer and the "gray zone" of turbulence: A critical review. *Journal of Geophysical Research: Atmospheres*, *125*(13), e2019JD030317. https://doi.org/10.1029/2019JD030317

Hooft, J. A. v., Baas, P., Tiggelen, M. v., Ansorge, C., & Wiel, B. J. H. v. d. (2019). An idealized description for the diurnal cycle of the dry atmospheric boundary layer. *Journal of the Atmospheric Sciences*, *76*(12), 3717–3736. https://doi.org/10.1175/JAS-D-19-0023.1

Huang, J., Lee, X., & Patton, E. G. (2011). Entrainment and budgets of heat, water vapor, and carbon dioxide in a convective boundary layer driven by time-varying forcing. *Journal of Geophysical Research*, *116*(D6), D06308. https://doi.org/10.1029/2010JD014938

Iacono, M. J., Delamere, J. S., Mlawer, E. J., Shephard, M. W., Clough, S. A., & Collins, W. D. (2008). Radiative forcing by long-lived greenhouse gases: Calculations with the AER radiative transfer models. *Journal of Geophysical Research*, *113*(D13), D13103. https://doi.org/10.1029/2008JD009944

Jonker, H. J. J., Heus, T., & Sullivan, P. P. (2008). A refined view of vertical mass transport by cumulus convection. *Geophysical Research Letters*, *35*(7), L07810. https://doi.org/10.1029/2007GL032606

Lilly, D. K. (1968). Models of cloud-topped mixed layers under a strong inversion. *Quarterly Journal of the Royal Meteorological Society*, *94*(401), 292–309. https://doi.org/10.1002/qj.49709440106

Lu, R., Lin, C., Turco, R., & Arakawa, A. (2000). Cumulus transport of chemical tracers: 1. Cloud-resolving model simulations. *Journal of Geophysical Research*, *105*(D8), 10001–10021. https://doi.org/10.1029/2000JD900009

McMichael, L. A., Yang, F., Marke, T., Löhnert, U., Mechem, D. B., Vogelmann, A. M., et al. (2020). Characterizing subsiding shells in shallow cumulus using doppler lidar and large-eddy simulation. *Geophysical Research Letters*, *47*(18), e2020GL089699. https://doi.org/10.1029/2020GL089699

Nicholls, S., & Lemone, M. A. (1980). The fair weather boundary layer in GATE: The relationship of subcloud fluxes and structure to the distribution and enhancement of cumulus clouds. *Journal of the Atmospheric Sciences*, *37*(9), 2051–2067. https://doi.org/10.1175/1520-0469(1980)037⟨2051:TFWBLI⟩2.0.CO;2

Ouwersloot, H. G., Moene, A. F., Attema, J. J., & Vilà-Guerau de Arellano, J. (2017). Large-eddy simulation comparison of neutral flow over a canopy: Sensitivities to physical and numerical conditions, and similarity to other representations. *Boundary-Layer Meteorology*, *162*(1), 71–89. https://doi.org/10.1007/s10546-016-0182-5

Ouwersloot, H. G., Vilà-Guerau de Arellano, J., H. van Stratum, B. J., Krol, M. C., & Lelieveld, J. (2013). Quantifying the transport of subcloud layer reactants by shallow cumulus clouds over the Amazon. *Journal of Geophysical Research: Atmospheres*, *118*(23), 13041–13059. https://doi.org/10.1002/2013JD020431

Pedruzo-Bagazgoitia, X., Jiménez, P. A., Dudhia, J., & Arellano, J. V.-G. d. (2019). Shallow cumulus representation and its interaction with radiation and surface at the convection gray zone. *Monthly Weather Review*, *147*(7), 2467–2483. https://doi.org/10.1175/MWR-D-19-0030.1

Pedruzo-Bagazgoitia, X., Ouwersloot, H. G., Sikma, M., Heerwaarden, C. C. v., Jacobs, C. M. J., & Vilà-Guerau de Arellano, J. (2017). Direct and diffuse radiation in the shallow cumulus–vegetation system: Enhanced and decreased evapotranspiration regimes. *Journal of Hydrometeorology*, *18*(6), 1731–1748. https://doi.org/10.1175/JHM-D-16-0279.1

Pino, D., Kaikkonen, J.-P., & Vilà-Guerau de Arellano, J. (2013). Quantifying the uncertainties of advection and boundary layer dynamics on the diurnal carbon dioxide budget. *Journal of Geophysical Research: Atmospheres*, *118*(16), 9376–9392. https://doi.org/10.1002/jgrd.50677

Pino, D., Vilà-Guerau de Arellano, J., & Kim, S.-W. (2006). Representing sheared convective boundary layer by zeroth- and first-order-jump mixed-layer models: Large-eddy simulation verification. *Journal of Applied Meteorology and Climatology*, *45*(9), 1224–1243. https://doi.org/10.1175/JAM2396.1

Pino, D., Vilà-Guerau de Arellano, J., Peters, W., Schröter, J., van Heerwaarden, C. C., & Krol, M. C. (2012). A conceptual framework to quantify the influence of convective boundary layer development on carbon dioxide mixing ratios. *Atmospheric Chemistry and Physics*, *12*(6), 2969–2985. https://doi.org/10.5194/acp-12-2969-2012

Rodts, S. M. A., Duynkerke, P. G., & Jonker, H. J. J. (2003). Size distributions and dynamical properties of shallow cumulus clouds from aircraft observations and satellite data. *Journal of the Atmospheric Sciences*, *60*(16), 1895–1912. https://doi.org/10.1175/1520-0469(2003)060⟨1895:SDADPO⟩2.0.CO;2

Ronda, R. J., Bruin, H. A. R. d., & Holtslag, A. a. M. (2001). Representation of the canopy conductance in modeling the surface energy budget for low vegetation. *Journal of Applied Meteorology and Climatology*, *40*(8), 1431–1444. https://doi.org/10.1175/1520-0450(2001)040⟨1431:ROTCCI⟩2.0.CO;2

Savre, J. (2022). What controls local entrainment and detrainment rates in simulated shallow convection? *Journal of the Atmospheric Sciences*, *79*(11), 3065–3082. https://doi.org/10.1175/JAS-D-21-0341.1

Siebesma, A. P., Bretherton, C. S., Brown, A., Chlond, A., Cuxart, J., Duynkerke, P. G., et al. (2003). A large eddy simulation intercomparison study of shallow cumulus convection. *Journal of the Atmospheric Sciences*, *60*(10), 1201–1219. https://doi.org/10.1175/1520-0469(2003)060⟨1201:ALESIS⟩2.0.CO;2

Siebesma, A. P., & Cuijpers, J. W. M. (1995). Evaluation of parametric assumptions for shallow cumulus convection. *Journal of the Atmospheric Sciences*, *52*(6), 650–666. https://doi.org/10.1175/1520-0469(1995)052⟨0650:EOPAFS⟩2.0.CO;2

Sikma, M., & Ouwersloot, H. G. (2015). Parameterizations for convective transport in various cloud-topped boundary layers. *Atmospheric Chemistry and Physics*, *15*(18), 10399–10410. https://doi.org/10.5194/acp-15-10399-2015

Sikma, M., & Vilà-Guerau de Arellano, J. (2019). Substantial reductions in cloud cover and moisture transport by dynamic plant responses. *Geophysical Research Letters*, *46*(3), 1870–1878. https://doi.org/10.1029/2018GL081236

Stevens, B. (2007). On the growth of layers of nonprecipitating cumulus convection. *Journal of the Atmospheric Sciences*, *64*(8), 2916–2931. https://doi.org/10.1175/JAS3983.1

Stull, R. B. (Ed.) (1988). *An introduction to boundary layer meteorology*. Springer Netherlands. https://doi.org/10.1007/978-94-009-3027-8

Tomassini, L., Willett, M., Sellar, A., Lock, A., Walters, D., Whitall, M., et al. (2023). Confronting the convective gray zone in the global configuration of the met office unified model. *Journal of Advances in Modeling Earth Systems*, *15*(5), e2022MS003418. https://doi.org/10.1029/2022MS003418

van der Laan-Luijkx, I. T., van der Velde, I. R., Krol, M. C., Gatti, L. V., Domingues, L. G., Correia, C. S. C., et al. (2015). Response of the Amazon carbon balance to the 2010 drought derived with CarbonTracker South America. *Global Biogeochemical Cycles*, *29*(7), 1092–1108. https://doi.org/10.1002/2014GB005082

van Stratum, B. J. H., Vilà-Guerau de Arellano, J., van Heerwaarden, C. C., & Ouwersloot, H. G. (2014). Subcloud-layer feedbacks driven by the mass flux of shallow cumulus convection over land. *Journal of the Atmospheric Sciences*, *71*(3), 881–895. https://doi.org/10.1175/JAS-D-13-0192.1

Verzijlbergh, R. A., Jonker, H. J. J., Heus, T., & Vilà-Guerau de Arellano, J. (2009). Turbulent dispersion in cloud-topped boundary layers. *Atmospheric Chemistry and Physics*, *9*(4), 1289–1302. https://doi.org/10.5194/acp-9-1289-2009

Vilà-Guerau de Arellano, J., Gioli, B., Miglietta, F., Jonker, H. J. J., Baltink, H. K., Hutjes, R. W. A., & Holtslag, A. A. M. (2004). Entrainment process of carbon dioxide in the atmospheric boundary layer. *Journal of Geophysical Research*, *109*(D18), D18110. https://doi.org/10.1029/2004JD004725

Vilà-Guerau de Arellano, J., Hartogensis, O. K., Boer, H. d., Moonen, R., González-Armas, R., Janssens, M., et al. (2024). CloudRoots-Amazon22: Integrating clouds with photosynthesis by crossing scales. *Bulletin of the American Meteorological Society*, *105*(7), E1275–E1302. https://doi.org/10.1175/BAMS-D-23-0333.1

Vilà-Guerau de Arellano, J., Kim, S.-W., Barth, M. C., & Patton, E. G. (2005). Transport and chemical transformations influenced by shallow cumulus over land. *Atmospheric Chemistry and Physics*, *5*(12), 3219–3231. https://doi.org/10.5194/acp-5-3219-2005

Vilà-Guerau de Arellano, J., Wang, X., Pedruzo-Bagazgoitia, X., Sikma, M., Agustí-Panareda, A., Boussetta, S., et al. (2020). Interactions between the Amazonian rainforest and cumuli clouds: A large-eddy simulation, high-resolution ECMWF, and observational intercomparison study. *Journal of Advances in Modeling Earth Systems*, *12*(7), e2019MS001828. https://doi.org/10.1029/2019MS001828

von Randow, C., Manzi, A. O., Kruijt, B., de Oliveira, P. J., Zanchi, F. B., Silva, R. L., et al. (2004). Comparative measurements and seasonal variations in energy and carbon exchange over forest and pasture in South West Amazonia. *Theoretical and Applied Climatology*, *78*(1), 5–26. https://doi.org/10.1007/s00704-004-0041-z